~~Asymmetric~~ Uneven Decline in the Hydrological Efficiency of China''s Natural and ~~Planted Forests~~Plantation ~~f~~Forests

Xiao Zhang[1,a] , Xinxiao Yu [a,b], Guodong Jia[a,b,*]

[a] *School of Soil and Water Conservation, Beijing Forestry University, Beijing 100083, China*

[b] *Key Laboratory of State Forestry Administration on Soil and Water Conservation, Beijing Forestry University, Beijing 100083, China*

Corresponding author: Guodong Jia (jgd304304@126.com)

Abstract

The vegetation transpiration fraction (TF) links terrestrial water and carbon cycles, yet the sensitivity of TF to changes in leaf area index (LAI)~~leaf area index (LAI) change~~ (θ) and its hydroclimatic controls remain poorly constrained, particularly in China's contrasting natural forests (NF) and plantation forests (PF). Using forest-type maps to identify natural forests (NF) and plantation forests (PF), together with GLEAM-derived evapotranspiration variables and ERA5-Land hydroclimatic data from 1990–2020, we quantified the spatiotemporal patterns of θ and evaluated the relative roles of soil moisture (SM) and vapor pressure deficit (VPD).~~spanning~~ We found that θ increased spatially from humid to semi-arid regions and was consistently higher in NF than in PF, but declined significantly over time in both forest types, with a larger decrease in PF. Along the joint SM–VPD gradient, θ exhibited a nonlinear response surface, with higher values concentrated under moderate SM and intermediate-to-high VPD conditions. Although VPD still explained a slightly larger share of the present spatial pattern of θ, the influence of SM strengthened over time, indicating increasing soil moisture limitation. Overall, China's forests appear to be shifting toward a more conservative water-use regime, in which the capacity of additional leaf area to enhance TF has weakened. These results provide new insights into how contrasting forest types regulate water use under concurrent warming and greening, with implications for climate-adaptive forest and water-resource management.~~The vegetation transpiration fraction (TF) is a key parameter linking terrestrial water and carbon cycles. Against the backdrop of global greening and climate change, the response of TF sensitivity to Leaf Area Index (LAI) changes (θ), and the relative roles of soil moisture (SM) and atmospheric drought (VPD), remain unclear, especially lacking a

~~systematic comparison between China's Natural Forests (NF) and Planted Forests (PF). This study utilized multi-source datasets from 1990–2020 (including forest types, GLEAM, and ERA5-Land) and employed methods including sliding windows, partial correlation, ridge regression, and mediation effect models to systematically analyze the spatiotemporal dynamics of θ in NF and PF, and to quantify the independent contributions and dynamic shifts of SM and VPD. Results show: 1) Forest θ spatially increases from humid to semi-arid regions (NF > PF); temporally, θ shows a widespread significant decline, with PF declining more (mean of −0.262 %·m^{-2}·m^{2}·decade^{-1}) than NF, especially in semi-arid/semi-humid transition zones. 2) θ exhibits a "hump-shaped" nonlinear response to the joint SM-VPD gradient, peaking at moderate SM and medium-high VPD. 3) The key hydrological drivers of θ are undergoing a dynamic shift from "atmospheric demand" (VPD) to "soil supply" (SM); the independent control of SM (β_{SM}) has significantly strengthened over time, while that of VPD (β_{VPD}) has weakened. 4) The two forest types show distinct response mechanisms: NF is more sensitive to VPD, while PF is more sensitive to SM stress. Overall, China's forests are shifting towards a more "conservative" water-use strategy, and the enhancing effect of LAI on TF has significantly weakened under strengthening SM constraints and VPD stress. The differentiated high sensitivity—NF to atmospheric drought and PF to soil drought—provides critical insights for forest water resource management and afforestation planning under future climate change scenarios.~~

Keywords:

natural forests, plantation forests, transpiration, leaf area index, soil moisture, vapor pressure deficit

1. Introduction

Terrestrial ecosystem evapotranspiration (E) is the primary pathway by which land surface moisture returns~~for land surface moisture to return~~ to the atmosphere~~,~~ ~~playing~~ and ~~it~~ thus plays a central role in the global water cycle (Liu et al., 2023; Sun et al., 2022). E comprises three components: soil evaporation (Es), vegetation canopy interception (Ei), and plant transpiration (T) (Niu et al., 2020; Wei et al., 2017). Among these, vegetation transpiration, ~~which transports water~~ by which water is released to the atmosphere through plant stomata, accounts for over 60% of total terrestrial E (Li et al., 2024; Wei et al., 2017). As transpiration is closely linked to ~~interrelated coupled with~~ both carbon assimilation and energy exchange, the vegetation transpiration fraction

(TF, defined as T/E) quantifies the contribution of vegetation to land–atmosphere water vapor flux and is a key indicator of vegetation–climate coupling strength (Schlesinger and Jasechko, 2014; Wei et al., 2017). Understanding changes in TF is crucial for revealing ecohydrological mechanisms and accurately predicting climate–change impacts.

Persistent climate warming and rising atmospheric CO_2 over the past few decades have driven global vegetation greening and altered ecosystem water balances (Denissen et al., 2022; Hu et al., 2023). The iIncreases in Leaf Aarea Index index (LAI) directly enhances canopy interception and transpiration potential—; global plant transpirationT is estimated to have increased by about 6% from 1990–2020, primarily as a consequence of increased LAIattributed to LAI enhancement (Chen et al., 2024). However, the positive effect of LAI on transpiration is dependsent on water availability: when soil moisture (SM) is scarce or atmospheric drought conditions (, often represented by vapor pressure deficit (, VPD), intensifiesy (often represented by Vapor Pressure Deficit, VPD) intensifies, plants regulateclose their stomata to suppress water loss, thereby reducing both transpiration and photosynthesis (Liu et al., 2020; Zahra et al., 2023). SM represents the supply-side constraint, whereashile VPD represents the atmospheric demand-side pull; these two factors often co-vary and impose compound can together impose a compound form of drought stress on ecosystems (Song et al., 2024). High VPD induces partial stomatal closure to prevent excessive water loss and hydraulic failure, causing transpiration rates per unit leaf area to saturate or even decline at high VPD under particularlyvery high VPD conditions (Grossiord et al., 2020; Novick et al., 2016). Therefore, even if as LAI increases, the additional leaf area struggles to further increase T under extreme atmospheric drought (Xu et al., 2023). Conversely, under moderate SM and appreciable atmospheric demand, vegetation can maintain both water supply and evaporative demand at levels favorable for that support transpiration, allowing increases in LAI to exert a stronger positive effect on TFConversely, under moderate SM and some atmospheric demand, vegetation has both sufficient water and high evaporative demand, maximizing water-carbon exchange efficiency; it is then that LAI increases most effectively boost TF (Liu et al., 2020). During extreme soil drought, increased surface sensible heat further dries the near-surface atmosphere, creating a positive SM–VPD feedback that accelerates drought evolution exacerbates drought conditions (Qing et al., 2022; Zhou et al., 2019). Accurately characterizing the response of TF to changes in LAI therefore requires a

unified framework that accounts for the synergistic and nonlinear effects of both soil water supply and atmospheric demand~~Thus, accurately understanding the response of TF to LAI changes changes in LAI requires considering comprehensive consideration of the synergistic effects and nonlinear impacts of both soil water supply and atmospheric demand within a unified framework~~ (Koehler et al., 2023). In recent years, discrepancies have ~~existed~~ emerged regarding the relative roles of SM and VPD: some studies ~~emphasize~~ have emphasized that atmospheric drought ~~is more critical in limiting~~ imposes greater limits on ecosystem water~~-~~ carbon cycles (Novick et al., 2016)~~; however,~~, whereas~~ile~~ others, after decoupling the coupled effects of VPD and SM~~their coupled effects~~, ~~find~~ have found that soil moisture is the dominant factor, especially in semi-arid regions, where SM typically imposes a stronger limitation on productivity (Liu et al., 2020). Because SM and VPD are often strongly correlated, quantifying their relative roles under coupled hydroclimatic conditions remains a central challenge in ecohydrological research. ~~Overall, SM and VPD are often highly correlated, intricately co-influencing interacting to impact plant transpiration and thus productivity. Disentangling their independent roles remains a challenge and a focal point in ecohydrological research.~~

Since the 1970s, China has implemented some of the world~~''~~s largest-scale afforestation and ecological restoration programs~~projects~~, increasing forest cover from ~~about~~ approximately 12% in the 1970s to over 22% in recent years (Cheng et al., 2025). China's forests now comprise extensive natural and planted forests. Natural forests are concentrated mainly in the mountainous regions of northeastern and southwestern China, whereas planted forests are more widespread in eastern, central, and southern China (Cheng et al., 2024b). Compared with natural forests, planted forests in China are more often younger, structurally simpler, and dominated by single-species or even-aged stands under more intensive management (Cheng et al., 2024a; Farooq et al., 2021).~~China~~''~~s current forests consist of vast newly planted and secondary forests, with characterized a unique coexistence cooccurrencecco-occurrence and distribution of Nnatural Fforests (NF) and Planted Forestsp (PF).: NF are area is mainly concentrated in the mountains of the Northeast and Southwest Northeast and Southwest China, characterized by complex age structures and deep-rooted tree species; PF are area is widespread inthroughout the plains and hills of the East, Central, and South China, often with high tree density, single species community compositions, and shallower rootsshallower roots, and

~~subject to various management activities like thinning and harvesting.~~ These differences in origin, structure, and water-use strategies may underlie~~y~~ ~~lead to~~ ~~significant~~ substantial disparities between NF and PF in soil water acquisition, stomatal regulation, and hydraulic safety margins, thereby leading to different responses of TF to changes in LAI~~consequently manifesting as different responses in LAI-induced TF changes~~ (hereafter~~i.e.~~, LAI–TF sensitivity, denoted as θ~~herein~~). Exploring these disparities between forest types can deepen the understanding of vegetation water-use mechanisms and improve regional water-resource management, afforestation benefit assessment, and climate-adaptive forestry strategies. However, systematic research on this issue is currently lacking. Existing studies have mostly examined the sensitivity of transpiration or productivity to drought stress at global or broad regional scales (Liu et al., 2020; Novick et al., 2016), or have focused on ecohydrological processes in specific arid regions, without a comparative assessment of θ across forest types along a unified climatic gradient. ~~Specifically: Are~~ This raises four interrelated questions: ~~-~~ (1) Are there systematic differences in θ between NF and PF along the climatic gradient from humid to semi-arid conditions? (2) How have these differences changed over the last 30 years? (3) Under coupled changes in SM and VPD, what are the relative roles of these two factors in shaping θ, and do these roles vary across climatic backgrounds or over time? (4) Through which hydrological pathways (SM and/or VPD) do changes in macroclimate, such as radiation, precipitation, temperature, and wind speed, indirectly affect θ? Addressing these questions will help fill important research gaps and deepen our understanding of forest–water relations under climate change.

The objectives of this study were to quantify the spatiotemporal patterns of transpiration sensitivity (θ) in China's natural forests (NF) and plantation forests (PF) from 1990 to 2020 and to identify the hydroclimatic controls underlying these patterns. To this end, we integrated multi-source remote-sensing and reanalysis data to derive growing-season LAI, evapotranspiration components, and meteorological variables for forest pixels at 0.1° resolution. We first used the aridity index (AI) framework to characterize the climatic background across four climatic zones and then focused the statistical analyses on the humid, semi-humid, and semi-arid zones to ensure comparability. We then applied complementary analytical approaches at different statistical scales: pooled spatial binning was used to characterize the response surface of θ along the joint SM–VPD

gradient and to compare spatial contrasts under comparable hydroclimatic backgrounds, whereas sliding-window partial correlation and ridge regression were used to quantify the independent temporal associations of SM and VPD with θ and their evolution over time. Finally, pathway analysis was used to decompose the indirect effects of macroclimate change on θ through local hydrological pathways. All trends were estimated using the Theil–Sen slope and evaluated with the Mann–Kendall test. We further assessed robustness through cross-product comparison and examined whether atmospheric CO_2 and stand age altered the main interpretation. Together, this framework was designed to reveal both the spatial heterogeneity and temporal evolution of hydroclimatic controls on θ in China's contrasting forest types.

2. Materials and methods

2.1. Data

We used datasets describing forest type, canopy structure, evapotranspiration components, hydroclimate, and several auxiliary background factors (Table 1). Forest type data were obtained from the 1990–2020 spatial distribution dataset of natural and plantation forests in China (Cheng et al., 2024b). This dataset was ~~generated~~ derived from Landsat imagery and extensive forest inventory samples using machine-learning classification and was resampled to 0.1° resolution to match the hydroclimatic datasets. Pixels with 100% coverage of either natural forest (NF) or plantation forest (PF) were treated as pure pixels, and only these pixels were included in all major analyses. – To maintain temporal consistency between forest masks and climate data, we adopted a period-based dynamic matching strategy. Specifically, forest maps for 1990, 1995, 2000, 2005, 2010, 2015, and 2020 were used to represent the periods 1990–1994, 1995–1999, 2000–2004, 2005–2009, 2010–2014, 2015–2019, and 2020, respectively.

LAI was derived from the GIMMS LAI4g dataset (Cao et al., 2023). The main evapotranspiration dataset used in this study was GLEAM v4.2a, from which transpiration (T), evapotranspiration (E), and soil moisture (SM) were extracted. GLEAM separately estimates the major components of terrestrial evaporation and provides both surface and root-zone soil moisture. In this study, SM refers to the root-zone soil moisture product, rather than surface soil moisture, because it more closely represents plant-available water relevant to transpiration regulation at the

seasonal to interannual scales considered here. In GLEAM, root-zone soil moisture is represented as a vegetation-accessible multi-layer soil profile constrained by assimilated surface observations, rather than as a single shallow soil layer. Near-surface meteorological variables, including air pressure (Pa), relative humidity (RH), air temperature (Ta), precipitation (P), dewpoint temperature (Td), wind speed (WS), net radiation (Rn), and potential evapotranspiration (PET), were obtained from ERA5-Land. All environmental variables were aggregated over the growing season (April–October) for 1990–2020, using only growing-season data and excluding non-growing-season observations. Means were used for state variables (e.g., LAI, SM, Ta, and VPD), whereas cumulative values were used for flux variables (e.g., E, T, and P).–

To evaluate the robustness of the estimated θ patterns and trends to data-product choice, we additionally used two alternative gridded products for cross-product comparison in supplementary analyses. One was the Simple Terrestrial Hydrosphere v2 (SiTHv2) product, which provides independent estimates of evapotranspiration and transpiration (Zhang et al., 2024). The other was the China terrestrial ecosystem transpiration fraction dataset (Niu et al., 2020), from which an alternative transpiration-fraction-based θ estimate was derived for comparison. These two datasets were used only for robustness assessment of θ, whereas all main calculations in the ~~manuscript~~ study were based on GLEAM.

To assess whether long-term changes in θ may also be modulated by non-hydroclimatic background factors, we further compiled several auxiliary datasets for supplementary analyses, including a global 1 ~~km~~ km– atmospheric carbon dioxide concentration dataset (Wang, 2025), a long-term reconstructed forest age dataset for China (Xia et al., 2024), and a 2020 forest age spatial distribution dataset for China (Cheng and Guo, 2024). These auxiliary datasets were resampled to 0.1° resolution and used only to assess whether CO_2 and stand age materially altered the observed θ patterns and trends. They were not included in the main analytical framework, in which the focus was on hydroclimatic controls.

Table 1. Data overview ~~**We used datasets covering multiple aspects including forest type, vegetation physiology, and hydroclimate (Table 1). Forest type data were from the 1990-2020 spatial distribution dataset of planted and natural forests in China published by Cheng et al. (2024). This dataset, based on Landsat satellite imagery combined with extensive forest**~~

~~inventory plot data, used machine learning algorithms like random forest to finely classify forests nationwide, effectively distinguishing between PF and NF types. To match climate data, this dataset was upscaled to 0.1° resolution using Average Resampling, yielding the coverage degree of PF and NF within each 0.1° pixel. We defined pixels with a coverage degree equal to 100% as pure pixels for the corresponding forest type, and all subsequent analyses were conducted on these pure pixels. To ensure temporal consistency between climate data and forest type data, we adopted a dynamic matching strategy based on time periods. Considering the relatively slow change in forest cover and data availability, we divided the 1990–2020 study period into 7 time segments, selecting a representative year's forest type data for each segment as the masking benchmark for all years' climate data within that segment. The forest type maps for 1990, 1995, 2000, 2005, 2010, 2015, and 2020 were used as representative products for the periods 1990–1994, 1995–1999, 2000–2004, 2005–2009, 2010–2014, 2015–2019, and 2020, respectively.~~

~~LAI data were sourced from the GIMMS LAI4g dataset (https://www.gleam.eu/). It is generated based on GIMMS NDVI3g records from AVHRR satellite observations, inverted through a trained neural network model.~~

~~T, E, SM were from the Global Land Evaporation Amsterdam Model (GLEAM) v4.2 dataset. GLEAM 4.2a calculates terrestrial evapotranspiration fluxes using an improved hybrid physical–machine learning framework, dividing processes like rainfall interception, crop water demand, and soil moisture dynamics into serial modules, and assimilating satellite observations (e.g., microwave soil moisture, vegetation optical depth) and reanalysis forcing data. To ensure the robustness of E, T, and the subsequently calculated TF and θ results, we simultaneously introduced the Simple Terrestrial Hydrosphere v2 (SiTHv2) product as an independent control. SiTHv2 (Zhang et al., 2024) is inverted from an ecohydrological energy balance model (Simple Terrestrial Hydrosphere) driven by reanalysis meteorology and constrained by satellite Vegetation Optical Depth (VOD). Our spatiotemporal comparison showed that the two products achieved moderate-to-high consistency in spatial patterns and interannual trends of TF and θ for both NF and PF (Fig. S1, S2), with regression slopes close to the 1:1 line and acceptable systematic bias, proving that the key conclusions of this study regarding TF and θ are robust to the data source.~~

~~Near-surface meteorological elements including pressure (Pa), relative humidity (RH), air temperature (Ta), precipitation (P), dewpoint temperature (Td), eastward and northward wind speed components (WSu, WSv), net radiation (Rn), and potential evapotranspiration (PET) were from the European Centre for Medium-Range Weather Forecasts (ECMWF) fifth-generation reanalysis (ERA5-Land, https://cds.climate.copernicus.eu/). It is generated through the advanced H-TESSEL land surface model, assimilating extensive ground and satellite observations globally, providing spatiotemporally continuous and physically consistent high-quality climate records.~~

~~Due to the temporal coverage limitations of the forest type data, all environmental variables were extracted for the growing season (April–October) from 1990–2020. Daily or monthly data were aggregated into growing season averages (e.g., Ta, VPD, SM) or cumulative values (e.g., E, T, P).~~

~~Table 1 Data overview~~

Variable	Data set	Resolution (spatial)	Resolution (temporal)	Time span	References
Forest type	Planted and natural forest maps in China from 1990 to 2020	1 km	5 years	1990–2020	Cheng et al., 2024b
LAI	GIMMS LAI4g	1/12°	15 day	1982–2020	Cao et al., 2023
E, T, SM	GLEAM v4.2a	0.1°	1 day	1980–2023	Miralles et al., 2025
Validation data	SiTHv2	0.1°	1 day	1982–2020	Zhang et al., 2024
	China terrestrial ecosystem transpiration fraction dataset	0.05°	8 day	1981–2015	Niu et al., 2020
Ta, Pa, RH, Td, P, PET, Rn, WS	ERA5-Land	0.1°	1 month	1950–2025	Muñoz-Sabater et al., 2021
CO_2	Global 1 km atmospheric carbon dioxide concentration dataset	1 km	annually	2003–2023	Wang, 2025
forest age	Long-term reconstructed forest age dataset for China	1 km	annually	1980–2015	Xia et al., 2024
	2020 forest age spatial distribution dataset for China	30 m	static	2020	Cheng et al.,2024a

LAI~~:~~, Leaf area index; E~~:~~, Evapotranspiration~~ration~~; T~~:~~, Transpiration; SM~~:~~, Root-zone soil moisture~~Soil moisture~~; Ta~~:~~, Air temperature; Td~~:~~, Dewpoint temperature; Pa~~:~~, Air pressure; P~~:~~,

Precipitation; PET~~,~~, Potential evapotranspiration; Rn~~,~~, Net radiation~~.~~; WS, wind speed.

2.2. Study region

Our study area covers~~is~~ terrestrial China, ~~which spans~~spanning temperate, subtropical, and tropical climate zones. The analysis focuses on~~subjects are~~ China~~'~~'s NF and PF. NF are mainly concentrated in the mountains of ~~the Northeast and Southwest~~ Northeast and Southwest China, whereas~~ile~~ PF are widely distributed across the plains and hills of ~~the East, Central, and South~~East, Central, and South China (~~Fig.~~Figure 1a). The vast majority of NF and PF are located in humid and semi-humid zones (~~Fig.~~Figure 2).

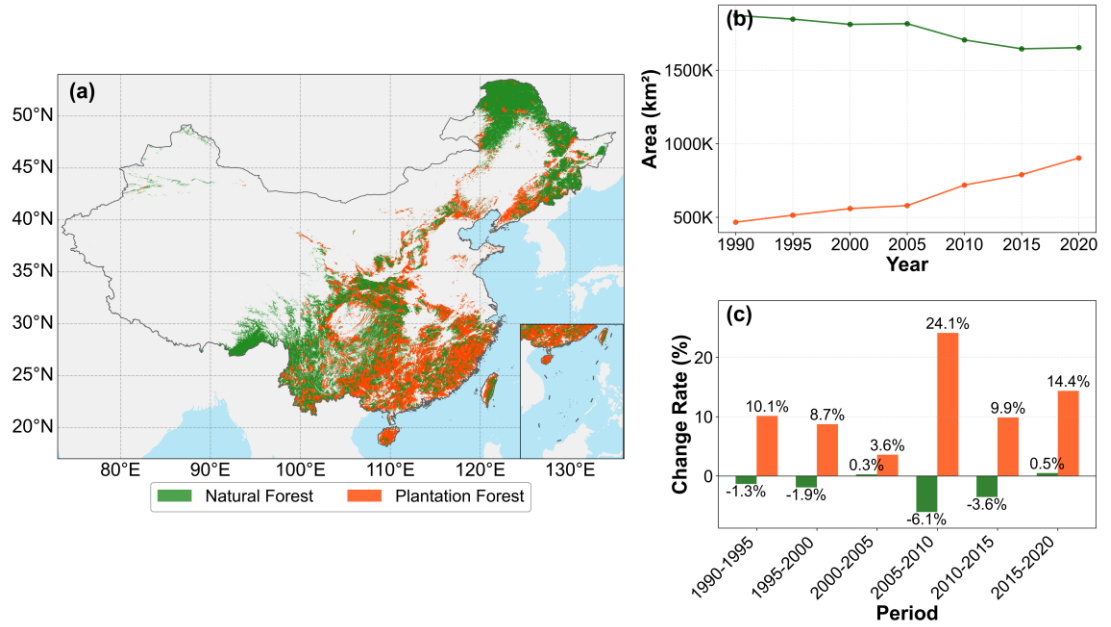

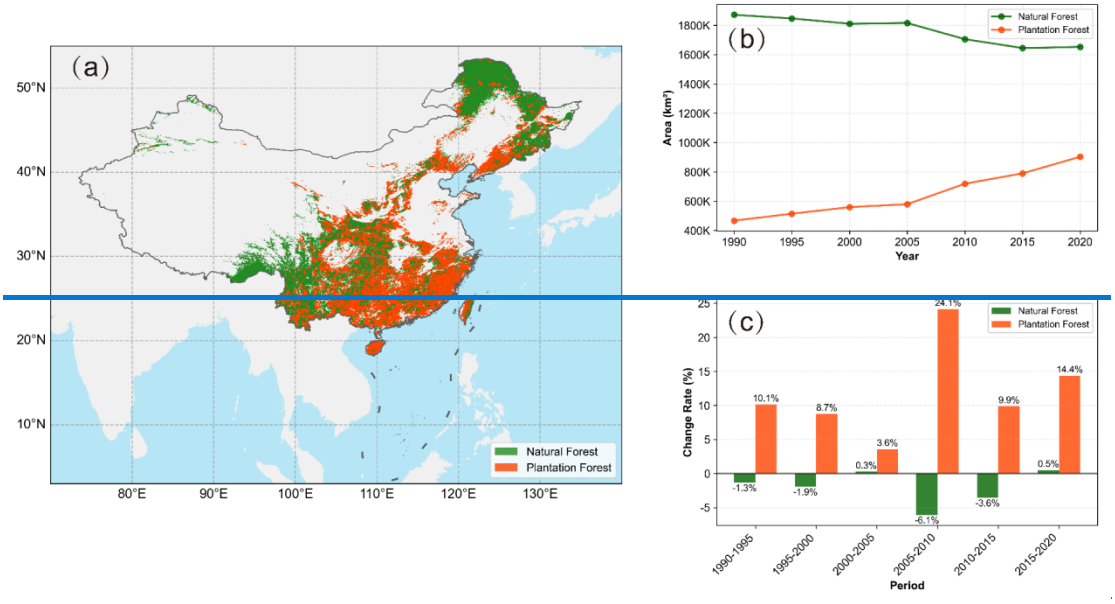

Figure 1. Spatiotemporal characteristics of China's natural forests (NF) and plantation forests (PF) from 1990 to 2020. ~~**Figure 1 Spatiotemporal characteristics of China's Natural Forests (NF) and Planted Forests (PF) from 1990–2020.**~~ (a) Average spatial distribution of NF (green) and PF (orange) in China from 1990–to 2020. (b) Dynamic changes in the area (km²) of NF and PF from 1990–to 2020. (c) Rate of change (%) in NF and PF area for each five-year period from 1990–2020.

2.2.1. Aridity index and analytical framework

We used the aridity index (AI) to characterize climatic background and to organize the spatial analyses within a unified framework. AI was defined as the ratio of annual potential evapotranspiration to annual precipitation, $AI = PET / P$. ~~Aridity Index and Analytical Framework~~

Based on the 1990–2020 multi-year mean AI, China was divided into four climatic zones: humid (AI < 1), semi-humid (1 ⩽ AI < 1.5), semi-arid (1.5 ⩽ AI < 4), and arid (AI ⩾ 4) (Zhu et al., 2022). This four-zone classification was used as the geographic framework for mapping and descriptive comparisons. Because forest samples in the arid zone were extremely sparse, subsequent statistical analyses were restricted to the humid, semi-humid, and semi-arid zones.

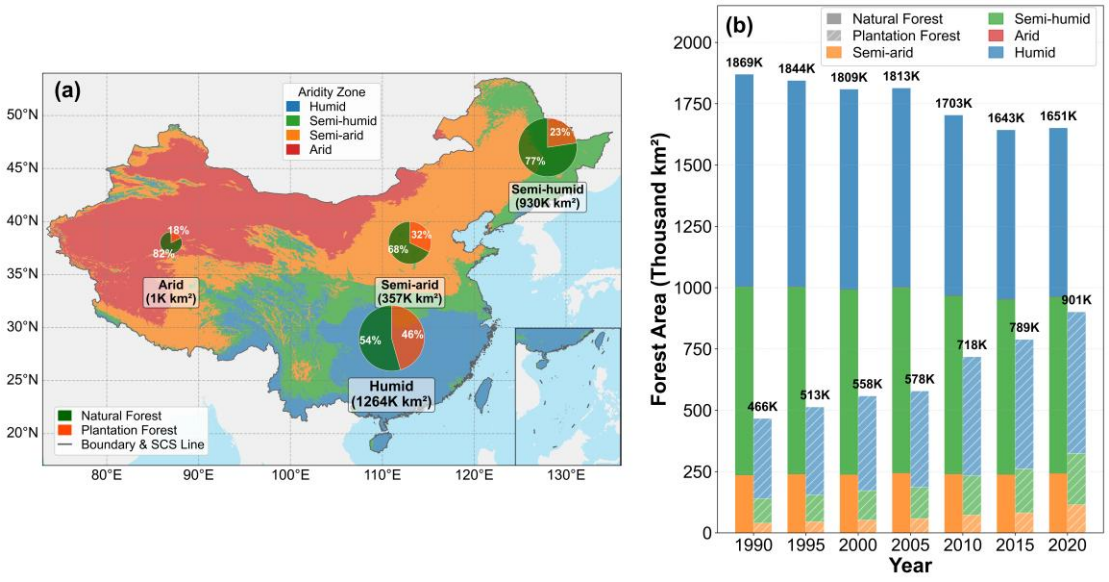

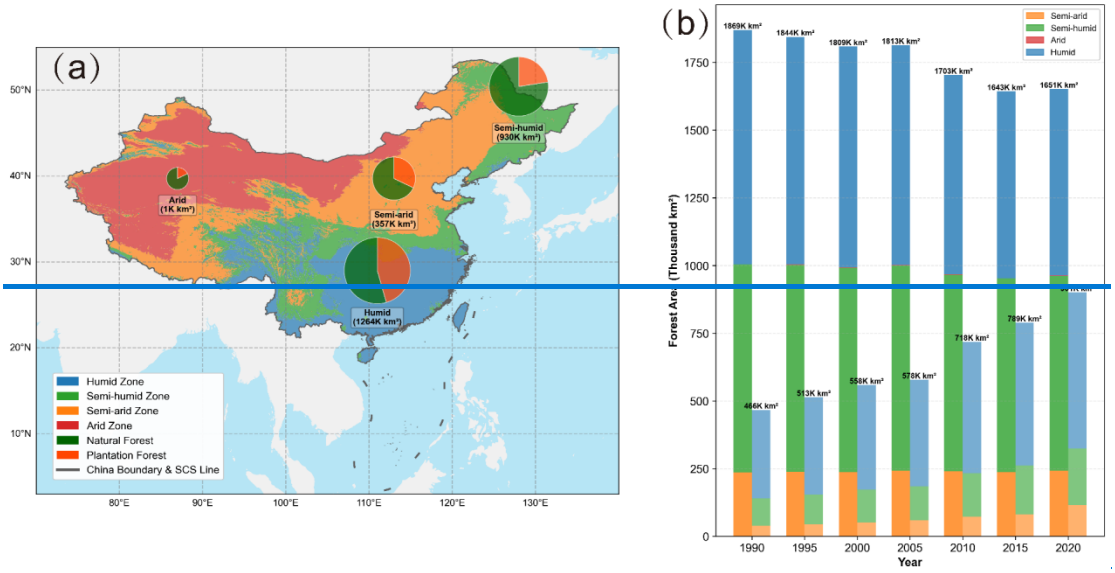

Figure 2. Spatiotemporal distribution and composition of forests in different climatic zones in China from 1990 to 2020. ~~**Figure 2 Spatiotemporal distribution and composition of forests in different climatic zones in China from 1990–2020.**~~ (a) Spatial distribution of the four climatic zones (humid, semi-humid, semi-arid, and arid) in China; the pie charts show the total forest area within each zone and its composition of natural forest (green) and planted forest (orange). (b) Dynamic changes in forest area in each climatic zone from 1990 to 2020. For each year, the left solid stacked bar represents natural forest (NF), and the right hatched stacked bar represents plantation forest (PF). Bar colors indicate the forest area contributed by different climatic zones. The value at the top of each year indicates the total national forest area, and labels with "K" denote 10^3 km^2 ~~Dynamic changes in forest area in each climatic zone from 1990 to 2020; the value at the top of the each bar represents the total national forest area (K km^2) for that year~~.

2.3. Methods

2.3.1. VPD ~~Calculation~~calculation

Vapor ~~Pressure Deficit~~ pressure deficit (VPD, hPa) is expressed, as follows, as the difference between saturation vapor pressure (P_s ~~P_s~~, hPa) and actual vapor pressure (P_w ~~P_w~~, hPa):

$$VPD = P_s - P_w \quad (1)$$

To calculate VPD, we used directly observed meteorological parameters, including air temperature (T_a ~~T_a~~, °C), relative humidity (RH ~~RH~~, %), and air pressure (P_a ~~P_a~~, hPa). P_s ~~P_s~~ was calculated using the improved Magnus equation (Yuan et al., 2019):

$$P_s = 6.112 \times f \times e^{\frac{17.67 \times T_a}{T_a + 243.5}} \quad (2)$$

~~where~~Here, f is the atmospheric pressure enhancement factor, which corrects for the effect of pressure on saturation vapor pressure in moist air (Buck, 1981). This coefficient is calculated using P_a ~~P_a~~ as follows:

$$f = 1 + 7 \times 10^{-4} + 3.46 \times 10^{-6} \times P_a \quad (3)$$

P_w ~~P_w~~ is then derived from P_s ~~P_s~~ and RH ~~RH~~ as follows :

$$P_w = P_s \times RH \times \frac{1}{100\%} \quad (4)$$

2.3.2. Sensitivity of ~~transpiration fraction~~TF to LAI

We define the transpiration fraction as~~The sensitivity (θ, %·m^{-2}·m^2) of the transpiration fraction (TF, %) to LAI changes is expressed by the following formulas~~:

$$TF = \frac{T}{E} \quad (5)$$

In this study, T and E were first aggregated from daily data to annual growing-season totals (April–October), and LAI was represented by the corresponding annual growing-season mean. TF was then calculated from these annual growing-season quantities, and all subsequent θ analyses were therefore conducted at the annual growing-season scale rather than at the daily or monthly scale.

Note that $TF \in (0,1)$ is bounded. To explicitly account for the inherent nonlinearity and saturation in the TF–LAI relationship, we estimated the sensitivity θ as a marginal response under a bounded nonlinear framework.

Within the full period (1990–2020) and within each 11-year moving window, we fit a quadratic model in logit space:

$$z = \mathrm{logit}(TF) = \ln\left(\frac{TF}{1-TF}\right) = a + b\left(LAI - LAI_{med}\right) + c\left(LAI - LAI_{med}\right)^2 \quad (6)$$

~~where~~ Here, LAI_{med} is the pixel-specific median LAI within the same period (median-centering ~~improves~~ was used to improve numerical stability). Prior to the logit transform, TF ~~is~~was clipped to $[\varepsilon, 1-\varepsilon]$ ($\varepsilon = 0.005$)~~in order~~ to avoid numerical singularities.

We then recovered $TF = 1/(1+e^{-z})$ and computed the marginal sensitivity as:

$$\theta = \frac{\partial TF}{\partial LAI} = TF\left(1-TF\right)[b + 2c\left(LAI - LAI_{med}\right)] \quad (7)$$

For ease of interpretation, Eq. (7) can be written as $\theta = \underbrace{TF(1-TF)}_{damping} \times \underbrace{[b + 2c(LAI - LAI_{med})]}_{\eta}$, ~~where~~in which the damping term reflects boundary effects and η represents the structural sensitivity in logit space.

To separate the ~~"~~position-dependent~~"~~ saturation effect from changes in the shape of the fitted TF-LAI relationship, we evaluated~~:~~ (i) θ_{total} at $LAI = LAI_{med}$, representing the sensitivity under the actual state of each pixel~~,~~ and (ii) θ_{clim} at a fixed reference LAI_{ref} (global median LAI), which removes the influence of shifting along the *TF*–LAI curve. ~~The~~ Additionally, the boundary component ~~is~~was quantified as~~:~~

$$\theta_{bound} = \theta_{total} - \theta_{clim} \quad (8)$$

We calculated θ at two time scales. (1) The full-period mean θ characterize~~d~~s the average state during 1990–2020. (2) The θ time series characterize~~d~~s decadal changes, generated using an 11-year moving window ~~and recorded by the center~~recorded for the central year (1995–2015), a data processing step that was also~~which is~~ used for subsequent trend and attribution analyses. Pixels with insufficient valid years and negligible LAI variability ~~are~~were excluded to ensure robustness.

2.3.3. Spatial association under the joint SM–VPD gradient: binning analysis

~~where T is vegetation transpiration (mm), and E is total surface evapotranspiration (mm). θ essentially reflects the average change in TF when LAI changes by one unit. To ensure computational accuracy, it is necessary to ensure that ΔLAI is not close to zero when deriving θ values. Therefore, when the LAI change trend within a specific time window fell in the -0.01 to 0.01 ($m^2\ m^{-2}$ $decade^{-1}$) range, the relevant data were excluded from the analysis. We calculated two time-scales of θ. The full-period mean θ characterizes the average state from 1990–2020, derived by linear regression fitting of the annual growing season mean TF and LAI data from 1990–2020 to obtain a single θ value representing the average condition. The θ time series characterizes decadal changes, generated using an 11-year sliding window method to calculate θ within the window~~

~~annually, creating a θ time series (1995–2015) marked by the window's center year, which was used for subsequent dynamic trend analysis.~~

~~2.3.3. Static Spatial Attribution: Binning Analysis~~

To assess the relative roles of SM and VPD in the spatial differentiation of θ, we applied a pooled spatial-binning analysis. Using all eligible pure NF and pure PF pixels as samples, we extracted the full-period mean θ, SM, and VPD values and *Z*-score standardized them~~standardized them by Z-score~~. To evaluate the relative effect of VPD under comparable SM backgrounds, denoted as Δθ(VPD|SM), pixels were first grouped into bins according to SM. Within each SM bin, the difference in mean θ between high- and low-VPD groups was calculated, and these differences were then averaged across bins. The relative effect of SM, denoted as Δθ(SM|VPD), was evaluated ~~analogously~~in the same way by binning pixels according to VPD and then comparing high- and low-SM groups within each bin. This approach ~~therefore~~thus summarize~~d~~s spatial contrasts under comparable hydroclimatic backgrounds using a control-variable logic. These analyses are complementary but not identical to the subsequent temporal attribution analyses~~:~~; specifically, the binning analysis characterize~~d~~s cross-site contrasts in θ across the long-term SM–VPD climate space, whereas the partial-correlation and ridge analyses quantifie~~d~~ within-pixel temporal associations of θ with SM and VPD.~~To quantify the independent contributions of SM and VPD to the spatial differentiation of θ, we used binning analysis. First, using all pure forest pixels in the study area as samples, we extracted their full-period mean θ, SM, and VPD, and Z-score standardized them. When assessing the independent effect of VPD, Δθ(VPD|SM), pixels were divided into bins based on SM values. Within each bin of similar SM, the difference in mean θ between high and low VPD groups was calculated. Finally, the differences from all bins were averaged to obtain the net effect of VPD after controlling for SM. The assessment of SM's independent effect, Δθ(SM|VPD), followed the same logic, binning by VPD and comparing high vs. low SM groups. This method spatially separates the independent contributions of the two factors using a "control variable" approach.~~

2.3.4. ~~Dynamic Temporal Attribution: Partial Correlation and Ridge Regression~~Dynamic temporal attribution: partial correlation and ridge regression

To investigate the pixel-scale temporal relationships of SM and VPD with θ ~~temporal relationships of SM and VPD with θ at the pixel scale~~, we used partial correlation and ridge regression based on the 1995–2015 11-year sliding-window series. This analysis was conducted at two levels. First, for each pixel, we calculated an overall partial correlation coefficient and ridge-regression coefficient ~~using~~based on the full 1995–2015 series, representing the average independent association of SM and VPD with θ ~~during~~ throughout that period after accounting for their covariation. Second, to evaluate ~~temporal evolution~~change over time, we performed a secondary sliding-window analysis on the same 1995–2015 series and generated time series of the coefficients themselves. Trends in these coefficient series were then used to infer whether the effects of SM and VPD ~~strengthened or weakened~~ became stronger or weaker over time. ~~In this way~~Thus, the first-level analysis describe~~d~~s the mean temporal attribution pattern, whereas the second-level analysis characterize~~d~~s its ~~evolution~~change over time.~~To investigate the control of SM and VPD on the temporal dynamics of θ at the pixel scale, we used partial correlation and ridge regression, both analyzing the 1995–2015 11-year sliding window time series data. This analysis had two levels: ① Static relationship analysis: First, for each pixel, we calculated an overall partial correlation coefficient and ridge regression coefficient using its complete 1995–2015 time series. This represents the average independent influence of SM and VPD on θ during this period. ② Dynamic trend analysis: To explore how this influence evolved, we applied a second-level sliding window analysis. Specifically, we used an 11-year window sliding over the 1995–2015 time series. Within each window, we calculated the partial correlation and ridge regression coefficients, thus generating a time series of the coefficients themselves for each pixel. Finally, we performed a trend analysis on this newly generated coefficient time series to reveal whether the independent influence or contribution of SM and VPD strengthened or weakened over time. The static relationship provides the full-period average independent impact, while the secondary sliding window tests whether these impacts evolved or underwent shifts; by treating the coefficients themselves as time series for trend estimation, we avoid masking heterogeneity from different periods within a single overall coefficient.~~

Partial correlation analysis: We calculated two pixel-wise partial correlation coefficients~~partial correlation coefficients pixel-wise~~: r(θ, SM|VPD) and r(θ, VPD|SM). The former represents the correlation between θ and SM after controlling for interannual VPD fluctuations, whereas the latter represents the correlation between θ and VPD after controlling for SM variability.~~coefficient coefficient~~ ~~The former represents the net correlation between θ and SM after removing the influence of interannual VPD fluctuations, indicating SM's independent influence; the latter similarly represents VPD's independent influence.~~

Ridge regression analysis: ~~Considering~~ Given the collinearity between SM and VPD, we further employed a ridge regression model, $\theta = \beta_{SM} \cdot SM + \beta_{VPD} \cdot VPD$, to more robustly quantify their relative contributions to θ. By introducing an L2 regularization term, ridge regression stabilizes coefficient estimates under multicollinearity. The regression was performed on standardized time series, and the resulting coefficients (β_{SM} and β_{VPD}) directly reflect the relative strengths of the SM and VPD effects. We further calculated the relative contribution (RC) of SM and VPD as $RC_{SM} = |\beta_{SM}| / (|\beta_{SM}| + |\beta_{VPD}|)$ and $RC_{VPD} = |\beta_{VPD}| / (|\beta_{SM}| + |\beta_{VPD}|)$, to ~~identify~~ determine the dominant hydrological driver at each pixel. To further diagnose multicollinearity between SM and VPD, we also calculated the variance inflation factor (VIF).~~Considering the collinearity between SM and VPD, we further employed a ridge regression model ($\theta = \beta_1 \cdot SM + \beta_2 \cdot VPD$) to more robustly quantify their independent contributions. Ridge regression, by introducing an L2 regularization term, effectively addresses multicollinearity, making the regression coefficients (β) more stable and reliable. We performed the regression on standardized time series, so the resulting standardized coefficients (β_1 and β_2) directly reflect the relative importance of SM (β_{SM}) and VPD (β_{VPD}). Based on this, we also calculated the Relative Contribution (RC), e.g., $RC_{SM} = |\beta_1| / (|\beta_1| + |\beta_2|)$, to intuitively determine which factor was dominant at each pixel.~~

To quantify temporal changes in θ and in the coefficient series derived from the 11-year moving-window analysis, we estimated trends using the Theil–Sen median slope estimator. Trend significance was assessed using the Mann–Kendall (MK) test (two-tailed, $\alpha = 0.05$). To reduce potential bias caused by temporal autocorrelation, the MK statistic was variance-corrected. The

same trend-analysis framework was applied consistently to all moving-window-derived time series used in the temporal attribution analysis.

2.3.5. ~~Mechanistic Attribution: Mediation Effect Analysis~~Pathway analysis of macroclimate effects on θ

To analyz~~s~~e the pathways through which macroclimate change may affect θ via local hydrological processes, we constructed a pathway model. The independent variable *X* ~~was~~ served as the climate-factor trend (including P, Ta, Rn, and WS), the mediator variable *M* ~~was~~ corresponded to the local water supply–demand status (SM and VPD trends), and the dependent variable *Y* ~~was~~ represented the θ trend. RH was not included separately because its effect on atmospheric water demand is already represented by VPD. Pathway analysis was used to partition the associations between macroclimate trends and θ into direct effects and indirect effects mediated through SM and VPD. The statistical significance of all pathway effects was tested ~~using~~ by bootstrap resampling (1000 iterations). Because SM and VPD may remain correlated under coupled hydroclimatic conditions, the pathway coefficients were interpreted as complementary association pathways rather than as a strict causal separation of two fully independent mediators. This interpretation was further evaluated using a supplementary mediator-specification comparison based on SM-only, VPD-only, and joint pathway models (Figure S19). The trends of P, Ta, Rn, WS, SM, VPD, and θ used in the pathway analysis were all estimated using the same Theil–Sen and variance-corrected Mann–Kendall framework described above.~~To test the causal chain of macro-climate change impacting θ through local hydrological processes, we constructed a mediation effect model. The independent variable X was the climate factor trend (P, Ta, Rn, WS), the mediator variable M was the local water supply-demand status (SM and VPD trends), and the dependent variable Y was the θ trend. The model analysis yielded the indirect effect transmitted via M. The significance of all mediation effects was tested using Bootstrap resampling (1000 times).~~

~~2.3.6. Trend analysis and testing~~Analysis and Testing

~~In this study, all time series (including coefficient series from based on the 11-year sliding window data) were uniformly analyzed using the Theil–Sen median slope estimation, and trend significance was assessed using the Mann–Kendall (MK) test (two-tailed, α = 0.05). To avoid bias from caused by temporal autocorrelation, the MK statistic was corrected usingsubjected to variance~~

~~correction. This setup approach ensures robustness to outliers, accounts for temporal autocorrelation,~~

~~and maintains consistency in.~~

3. Results

3.1. ~~Spatiotemporal differentiation and trends of θ~~Spatiotemporal patterns and long-term trends of θ

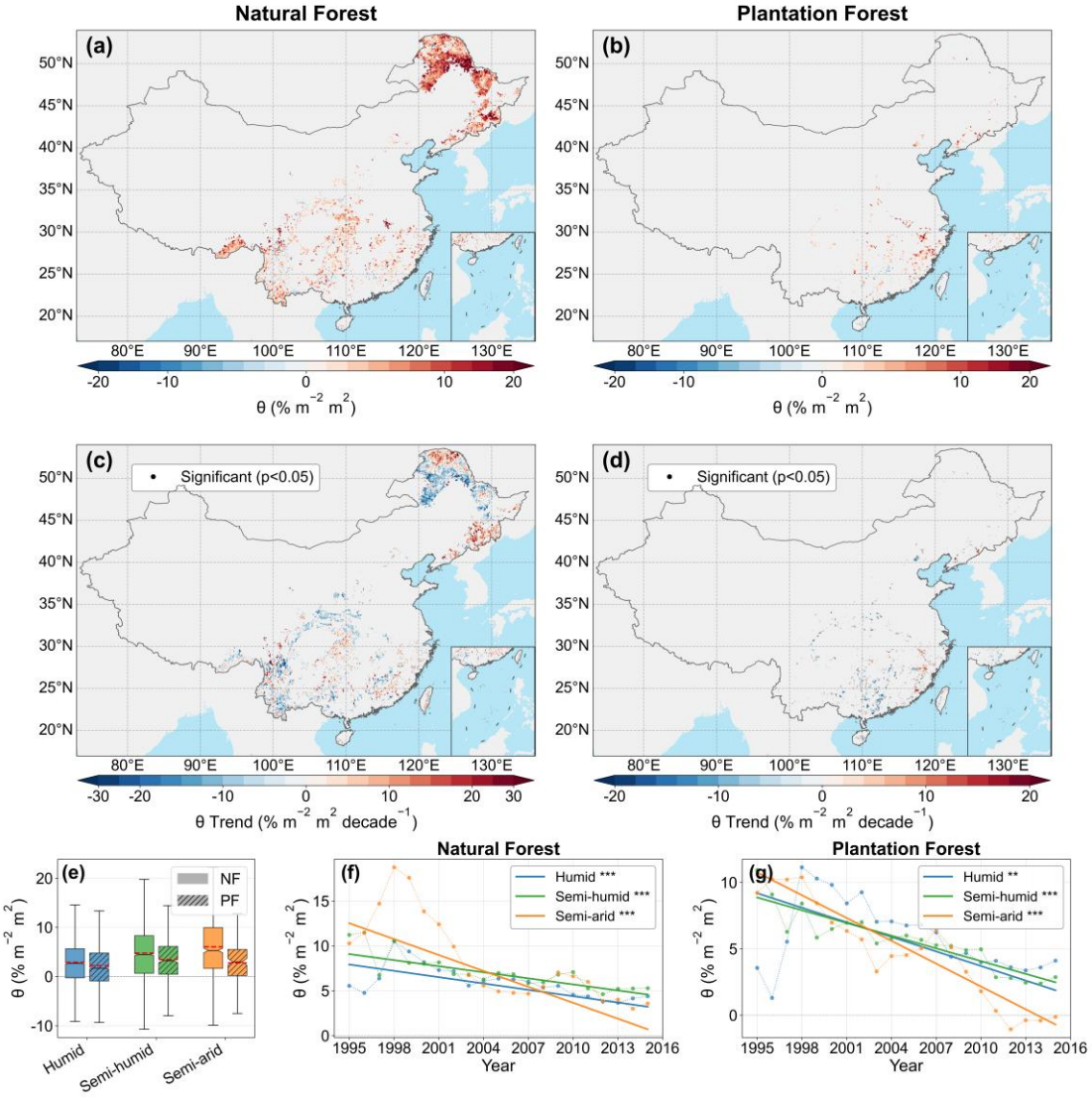

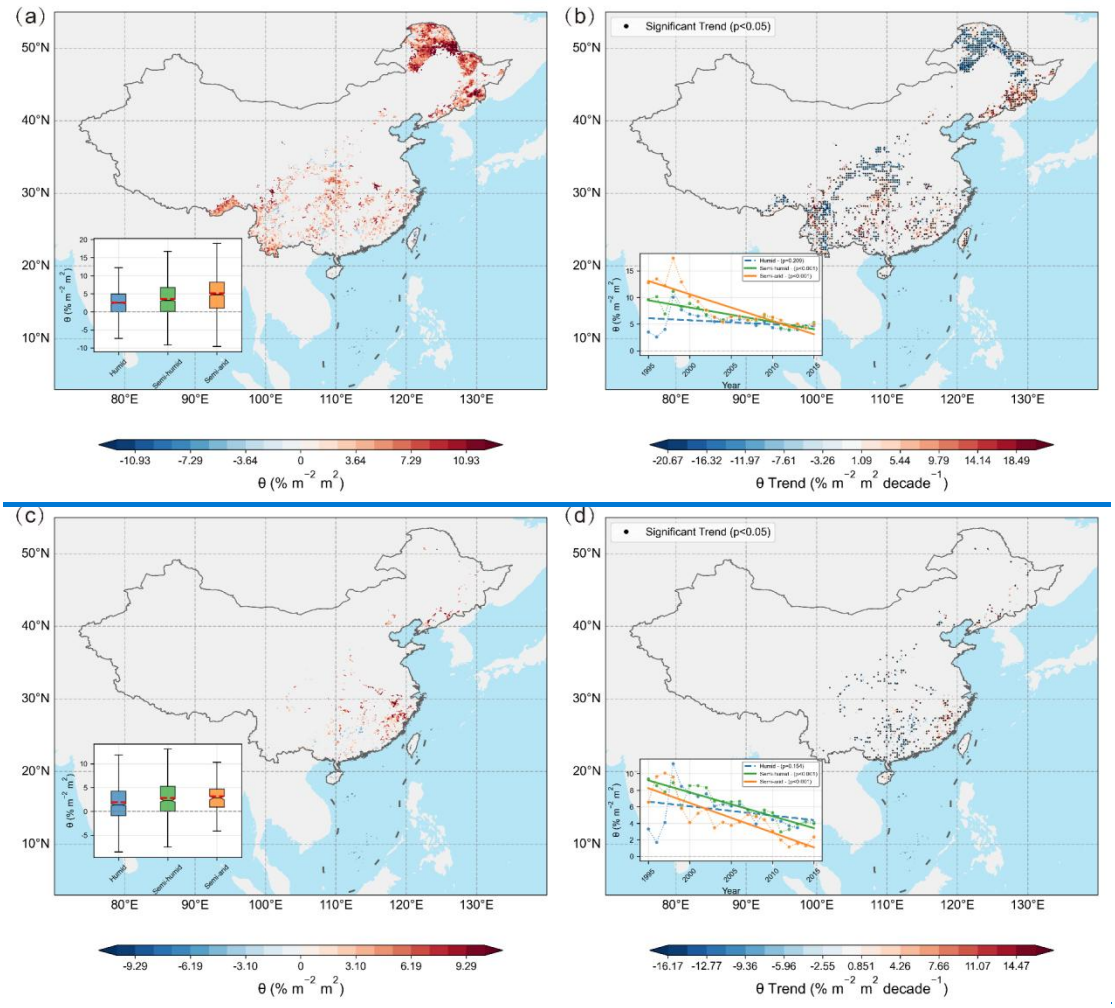

Figure 3. Spatiotemporal patterns and long-term trends of LAI ~~(LAI)~~ –TF –sensitivity (θ) in China's natural forests (NF) and plantation forests (PF) during the 1990–2020 growing seasons. (a) and (b) show the multi-year mean spatial distribution of θ for NF and PF, respectively, derived from the overall logit–quadratic model using TF_E (c) and (d) show the corresponding long-term trends in θ estimated from the 11-year moving-window time series using the Theil–Sen slope; black dots indicate significant trends based on the Mann–Kendall test ($p < 0.05$). (e) shows the distribution of θ across climatic zones (~~H~~humid, ~~S~~semi-humid, and ~~S~~semi-arid) for NF and PF. (f) and (g) show the temporal evolution of zone-averaged θ for NF and PF, respectively, with Theil–Sen trend lines overlaid.~~**Figure 3 Spatiotemporal dynamics of LAI-TF sensitivity (θ) for China's Natural Forests (NF) and Planted Forests (PF) during the 1990-2020 growing season.** (a) and (c) show the multi-year mean θ spatial distribution for NF(a) and PF(c) during the growing season (April-October) from 1990-2020. The bottom-left boxplots show the statistical distribution of θ values for both forest types in different climatic zones (Humid, Semi-humid, Semi-arid). (b) and (d)~~

~~show the spatial distribution of the θ interannual change trend for NF(b) and PF(d) from 1990–2020. The trend (%·m⁻²·m²·decade⁻¹) is based on the θ time series calculated using an 11-year sliding window and estimated by the Theil–Sen slope. Black dots indicate significant trends ($p<0.05$) by the Mann–Kendall test. The bottom-left line plots show the spatially averaged θ interannual time series for each climatic zone, overlaid with linear trend lines (solid lines for significant trends, dashed for non-significant).~~

Mean θ showed clear spatial heterogeneity and was consistently higher in NF than in PF (Figure 3a, b, e). High-θ areas in NF were concentrated mainly within the semi-arid to semi-humid transition belt, whereas PF showed a distinctly more fragmented pattern. During 1990–2020, growing-season θ declined widely in both forest types, with a stronger mean decline in PF than in NF (Figure 3c, d). Significant negative trends were concentrated mainly in semi-humid and semi-arid transition regions, while humid regions showed weaker negative trends. The zone-averaged time series further confirmed that θ decreased significantly across climatic zones in both forest types, with the strongest declines occurring under drier climatic conditions (Figure 3f, g). Overall, the marginal enhancement of TF by increasing LAI weakened over the past three decades, especially in ~~plantation forests~~ PF and in relatively dry regions.~~The multi-year mean θ spatially increases from the humid zone to the semi-humid and then to the semi-arid zone (Fig. 3a, 3c), with NF θ being significantly higher than PF θ ($p < 0.001$); this difference widens with increasing aridity. The high-value belt for NF is mainly concentrated in the semi-arid to semi-humid monsoon margin and ecological transition zones (e.g., North China, northern Loess Plateau, and western Northeast China). PF, though dispersed, shows relatively high values in the southeastern coast and the Northeast. θ exhibits a widespread significant decreasing trend during the study period (Fig. 3b, 3d), which is particularly prominent in the semi-arid and semi-humid transition zones ($p < 0.001$), while the humid zone is relatively stable. Although NF has a higher initial θ, PF shows a larger average decline (approx. −0.262 vs. −0.142 %·m⁻²·m²·decade⁻¹). Pixels with significant decline largely overlap with the initial high-value areas, suggesting a systematic weakening in these sensitive zones over the past 30 years.~~

3.2. ~~Control of Water Stress Factors (SM and VPD) on θ~~Hydroclimatic controls of θ: SM and VPD

3.2.1. Response of θ to the joint SM–VPD gradient~~Response Pattern of θ to the SM-VPD Joint Gradient~~

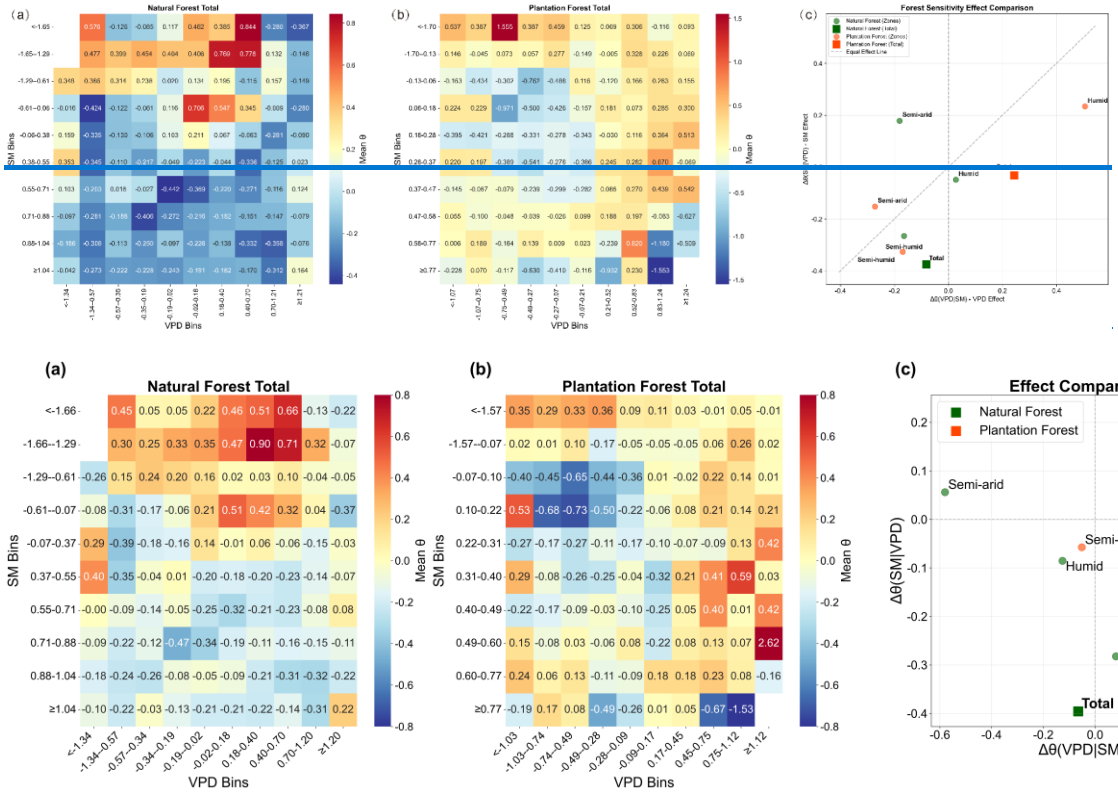

Figure 4. Pooled spatial binning analysis of LAI—TF sensitivity (θ) under the joint soil moisture (SM)–vapor pressure deficit (VPD) ~~SM–VPD~~ gradient during the 1990–2020 growing seasons. (a) and (b) show the mean standardized θ values in 10 × 10 SM–VPD bins for natural forests (NF) and plantation forests (PF), respectively; only bins with sample size ≥ 10 are shown. (c) shows the relative effects of VPD and SM as indicated by Δθ(VPD|SM) and Δθ(SM|VPD), calculated from the top 20% versus bottom 20% contrasts within each bin and then averaged across bins. Circles denote climatic zones ~~and~~, while squares denote the national total. θ was Z-score standardized in this analysis.

~~Figure 4 Pooled spatial analysis and independent effect comparison of forest LAI—TF sensitivity (θ) under the SM-VPD joint gradient for the 1990-2020 growing season. (a) Natural Forest (NF), (b) Planted Forest (PF): All pure forest pixels were binned into 10×10 bins based on SM and VPD deciles. Each cell shows the mean θ for that bin (only bins with sample size ≥10 are shown). (c) Independent effect comparison: Within each SM bin, the difference in mean θ between the top 20% and bottom 20% VPD groups was averaged across bins to get Δθ(VPD|SM); similarly, Δθ(SM|VPD)~~

~~was derived by comparing SM groups within each VPD bin. Circles represent arid/humid zones, squares represent the national total; the dashed line is the 1:1 line (Δθ(VPD|SM)=Δθ(SM|VPD). (θ is dimensionless if Z-score standardized).~~

~~To explore the universal impact patterns of SM and VPD on θ, we first pooled all forest pixels nationally via binning analysis to construct a response surface of θ to the 2D SM-VPD environmental gradient. θ is suppressed at extreme SM and VPD values but peaks under moderate SM and medium-high VPD conditions, forming a "hump-shaped" response pattern (amplified in the middle, attenuated at the extremes) (Fig. 4a, b). The independent effect comparison further shows (Fig. 4c) that in the semi-arid zone, Δθ(SM|VPD) is significantly greater than Δθ(VPD|SM), meaning SM is the dominant factor for θ changes. In the humid zone, VPD's relative importance increases significantly, with the semi-humid zone showing transitional characteristics. In the type comparison, NF exhibits a higher peak and a broader sensitive range in most SM-VPD combinations, while PF shows a narrower response window and earlier sensitivity attenuation (lower θ in high/low-end bins), suggesting PF has a weaker marginal response to extreme wet or dry - high VPD conditions.~~Pooled binning analysis showed that θ varied nonlinearly along the joint SM–VPD gradient in both forest types, with relatively high values occurring under intermediate SM and moderate-to-high VPD conditions, and lower values toward both the wet/low-VPD and dry/high-VPD ends of the gradient (Figure 4a,b). The contrast analysis further revealed clear differences in the relative effects of SM and VPD (Figure 4c). At the national scale, NF showed a much stronger SM-related contrast than VPD-related contrast [Δθ(SM|VPD) = −0.396 ~~vs.~~versus Δθ(VPD|SM) = −0.065], whereas PF showed the opposite pattern, with a much stronger VPD-related contrast [Δθ(VPD|SM) = 0.228 ~~vs.~~versus Δθ(SM|VPD) = 0.009]. Across climatic zones, NF exhibited stronger VPD-related contrasts in the humid and semi-arid zones but stronger SM-related contrasts in the semi-humid zone. In contrast, PF was mainly VPD-dominated in the humid and semi-arid zones, while both contrasts were relatively weak in the semi-humid zone. Within the pooled spatial-binning framework, these results indicate that the relative roles of soil water supply and atmospheric demand differed markedly between NF and PF. Zone-specific pooled SM–VPD binning patterns for NF and PF are shown in Figures S14 and S15, respectively.

3.2.2. Dynamic evolution of the independent effects of SM and VPD~~Dynamic Evolution of SM and VPD Independent Control~~

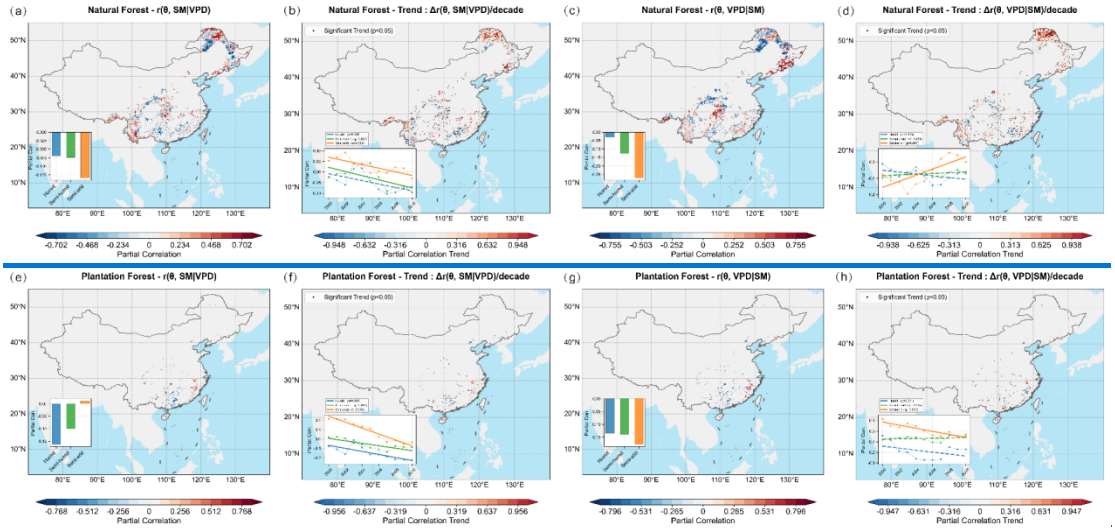

Partial-correlation analysis ~~showed~~revealed that the independent associations of θ with both SM and VPD were predominantly negative~~,~~ and were generally stronger in PF than in NF (Figure 5). At the national scale, the mean values of r(θ, SM|VPD) and r(θ, VPD|SM) were −0.0725 and −0.0992 in NF, compared with −0.1517 and −0.1630 in PF, respectively, indicating slightly stronger VPD-related associations in both forest types and overall stronger hydroclimatic constraints in PF. Across climatic zones, the strongest negative partial correlations in NF occurred in the semi-arid zone, especially for VPD, whereas PF showed consistently negative correlations across all zones. The temporal analyses further revealed spatially heterogeneous changes in these relationships (Figure 6). In NF, the SM-related partial correlation became less negative in the humid and semi-arid zones, while the VPD-related partial correlation also became less negative in the semi-humid zone. In PF, the SM-related partial correlation became more negative in the semi-humid and semi-arid zones, whereas the VPD-related partial correlation became less negative in the semi-humid zone. Overall, both SM and VPD constrained θ, but the constraints were generally stronger in PF, and their temporal changes were regionally differentiated rather than spatially uniform.

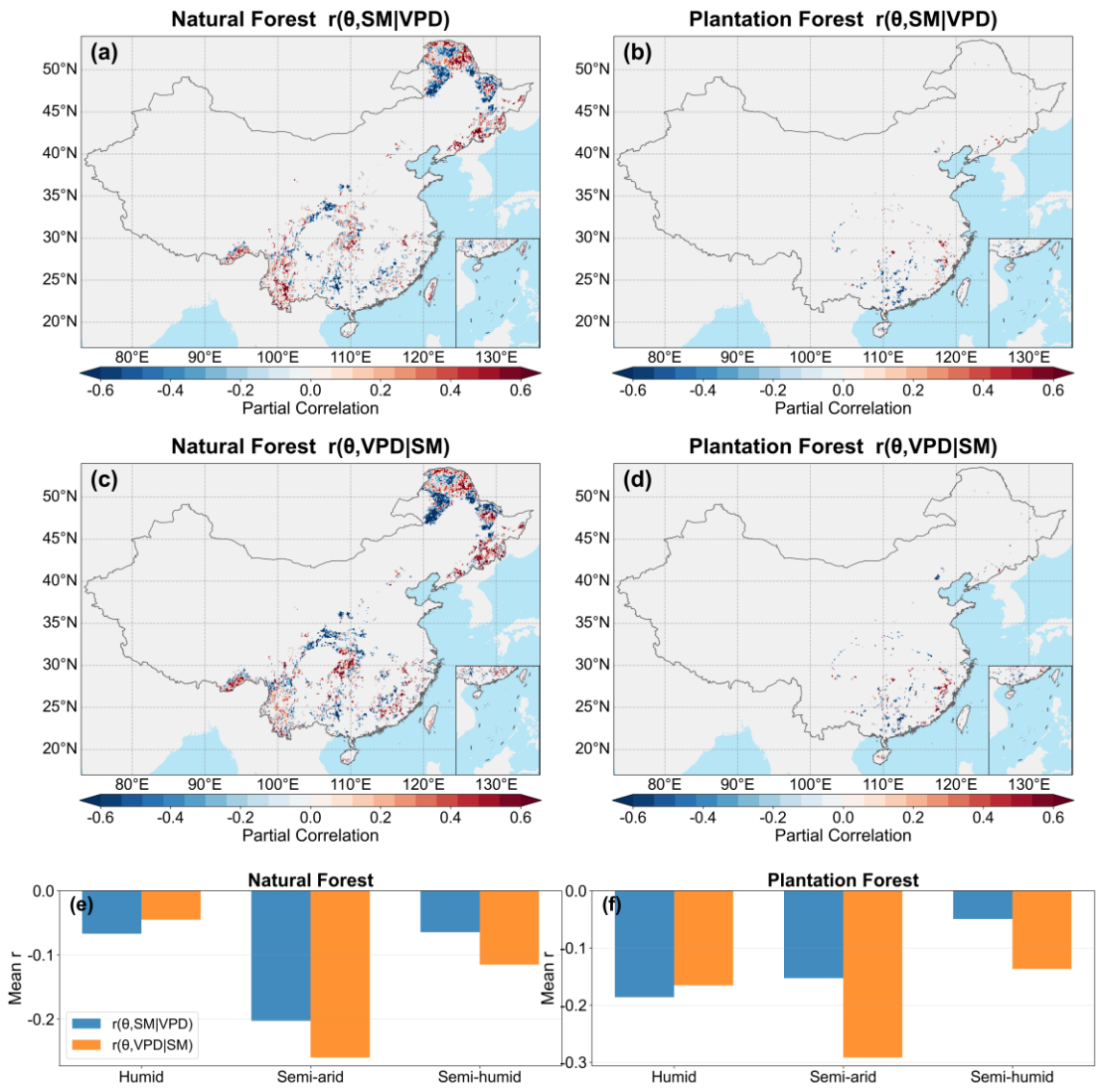

~~Figure 5 Partial correlation of forest LAI-TF sensitivity (θ) with SM/VPD and its decadal trends. (a) NF r(θ, SM | VPD) spatial distribution; (b) NF Δr(θ, SM | VPD) trend (change per decade); (c) NF r(θ, VPD | SM); (d) NF Δr(θ, VPD | SM) trend; (e–h) corresponding results for PF. Partial correlation coefficients reflect the linear association strength between θ and the target variable after controlling for the other variable. Trends were estimated using Theil–Sen slope, significance by Mann–Kendall test, with black dots marking $p<0.05$. Inset bar plots show mean partial correlation coefficients for arid/humid zones; inset line plots show temporal trends of spatially averaged partial correlation coefficients for each climatic zone, overlaid with linear trend lines (solid for significant, dashed for non-significant).~~

~~Based on the θ from the sliding window (1995–2015), the independent effects of SM and VPD on θ are predominantly negative. The national average for NF was r(θ, SM|VPD) = −0.079 and r(θ,~~

~~VPD|SM) = −0.105. PF's negative correlation was stronger, at r(θ, SM|VPD) = −0.1412 and r(θ, VPD|SM) = −0.1388. Spatially, negative correlation areas are mainly in Southern China, while positive correlation areas are concentrated in the Northeast (Fig. 5a, c).~~

~~The two forest types show different dependencies on the arid/humid gradient. For NF, the negative control of both SM and VPD gradually weakens from the semi-arid to the humid zone, with the VPD effect being particularly obvious (mean r(θ, VPD|SM) weakens from −0.2710 in the semi-arid zone to −0.0294 in the humid zone). This indicates that in humid regions, NF sensitivity (θ) is largely unaffected by VPD's independent influence. However, PF shows the opposite pattern: its sensitivity (θ) is under stronger negative constraint from both SM and VPD in humid regions (means −0.1632 and −0.1351, respectively), while in the semi-arid zone, SM's independent influence even turns slightly positive (mean 0.0118) (Fig. 5e, g inset plots).~~

~~The negative control of SM (i.e., r(θ, SM|VPD)) shows a negative trend (Δr<0) in most of Southern China, meaning the negative correlation is strengthening; this phenomenon is particularly prevalent in PF (Fig. 5b, f). In contrast, the control of VPD (i.e., r(θ, VPD|SM)) shows a widespread weakening trend (positive trend) nationally. Large areas of significant positive trends appear in both NF and PF in Eastern and Southern China (Fig. 5d, h). The time-series analysis (inset plots) clearly reveals that in humid and semi-humid regions, the negative correlation of SM's influence deepens over time (trend line slopes down), while the negative correlation of VPD's influence gradually weakens, even turning positive (trend line slopes up). This "one strengthens, one weakens" dynamic evolution reveals that the forest's response pattern to water stress may be undergoing a systematic shift—from being more constrained by atmospheric drought (VPD) in the past to being more constrained by soil drought (SM) today.~~

Figure 5. Spatial distribution and zonal means of partial correlations between forest LAI–TF sensitivity (θ) and hydroclimatic factors during the growing season from 1995 to 2015. (a) and (b) show the spatial patterns of r(θ, SM|VPD) for natural forests (NF) and plantation forests (PF), respectively; (c) and (d) show the corresponding patterns of r(θ, VPD|SM). (e) and (f) show the mean partial correlations across climatic zones. All variables were *Z*-score standardized before analysis, and pixels with fewer than 10 years of valid data were excluded.

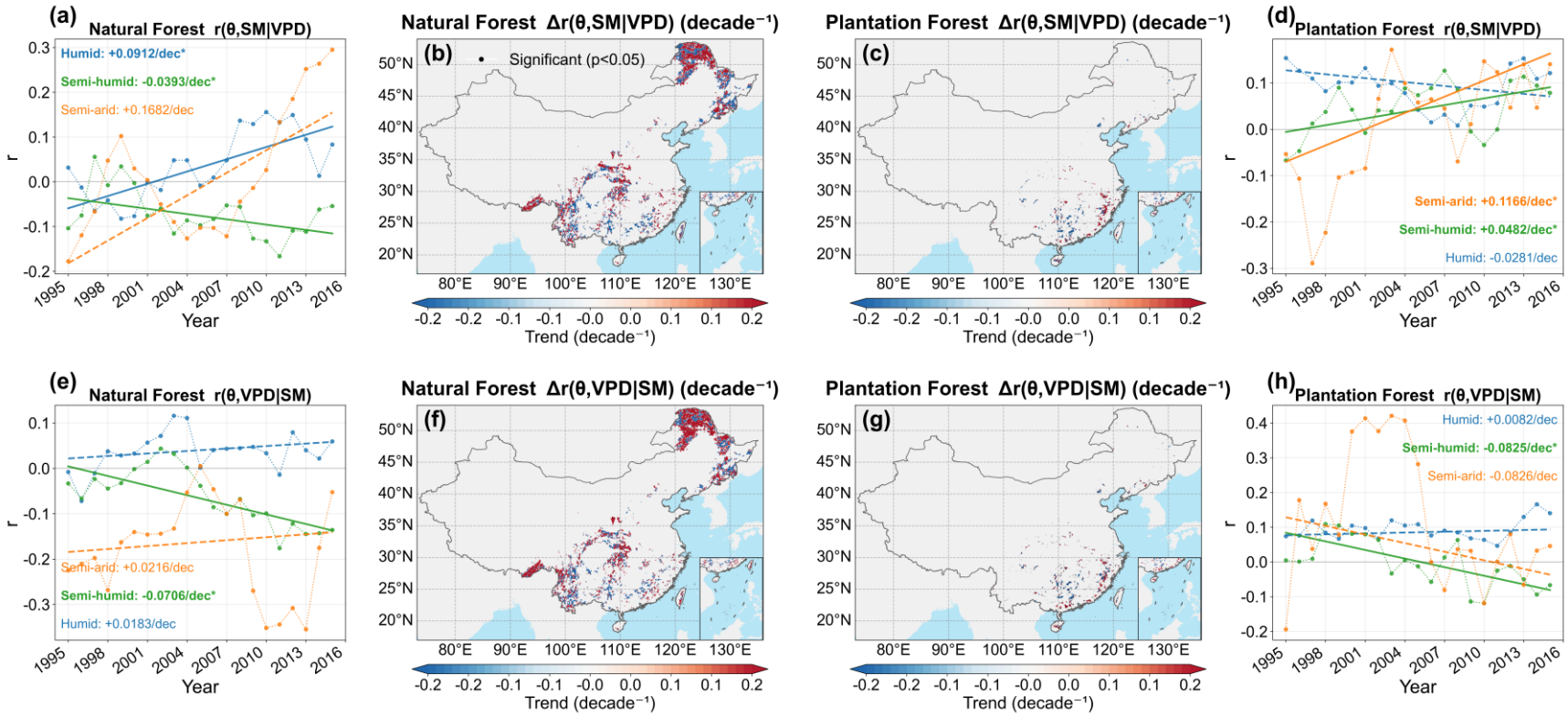

Figure 6. Temporal evolution and spatial trends of partial correlations between forest LAI–TF sensitivity (θ) and hydroclimatic factors during the growing season from 1995 to 2015. (a) and (d) show the temporal evolution of zone-averaged r(θ,SM | VPD) for NF and PF, respectively; (b) and (c) show the corresponding spatial trends. (e) and (h) show the temporal evolution of zone-averaged r(θ,VPD | SM) for NF and PF, respectively; (f) and (g) show the corresponding spatial trends. Trend slopes were estimated using the Theil–Sen estimator, and significant pixels ~~based on~~ according to the variance-corrected Mann–Kendall test ($p < 0.05$)

are ~~marked by~~indicated by~~as~~ black dots.

3.2.3. Quantification and sSpatiotemporal hHeterogeneity of dDominant hHydrological dDrivers

Ridge regression showed that both SM and VPD were generallyexerted negative effects onwere negatively associated with θ, but the magnitude was usually stronger for VPD (Figure 7). At the national scale, both NF and PF remained slightly more VPD-dominated in terms of the present spatial pattern, with mean relative contributions of VPD of 0.541 and 0.534 in NF and PF, respectivelyin NF and 0.534 in PF. Consistently, VPD-dominated pixels accounted for 57.1% of all NF pixels and 57.0% of all PF pixels, compared with 42.9% and 43.0%, respectively, for SM-dominated pixels for SM-dominated pixels, respectively. The relative-contribution and dominance statistics therefore consistently indicated a modest present-day advantage of VPD over SM, particularly in the semi-arid zone. The trend analysis further indicated a general strengthening of the SM effect and a weakening of the VPD effect in several regions, especially across semi-humid to semi-arid areas (Figure 8). Within the pixel-wise temporal analysis, these results suggest that VPD currently explained a slightly larger share of the spatial pattern of θ, whereas the relative role of SM has increased over time. RC and VIF diagnostics supported the robustness of this interpretation (Figure S16).

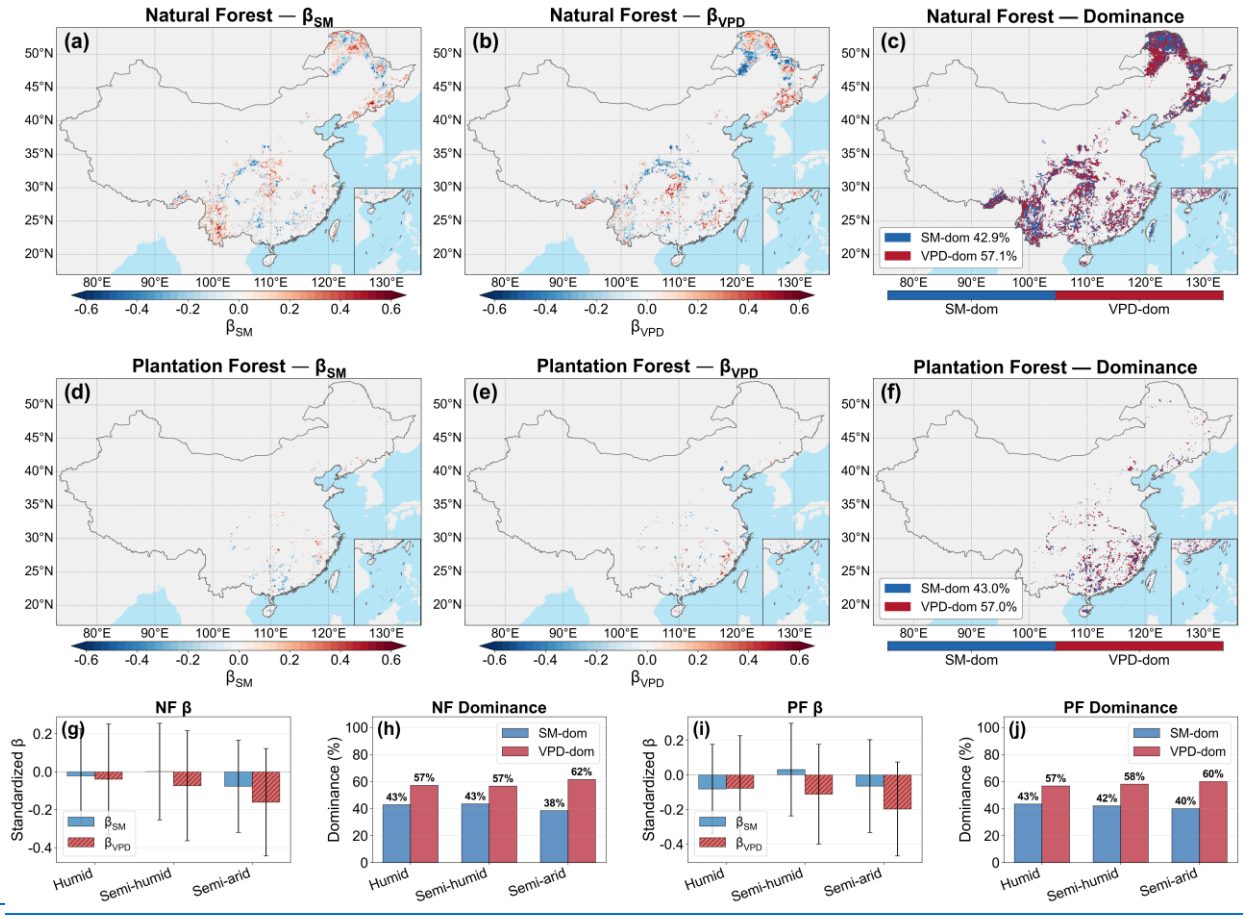
Natural Forest — β_{SM}
Natural Forest — β_{VPD}
Natural Forest — Dominance
(a)
(b)
(c)
SM-dom 42.9%
VPD-dom 57.1%
SM-dom
VPD-dom
β_{SM}
β_{VPD}
Plantation Forest — β_{SM}
Plantation Forest — β_{VPD}
Plantation Forest — Dominance
(d)
(e)
(f)
SM-dom 43.0%
VPD-dom 57.0%
NF β
NF Dominance
PF β
PF Dominance
(g)
(h)
(i)
(j)
Standardized β
Dominance (%)
SM-dom
VPD-dom
Humid
Semi-humid
Semi-arid
43%
57%
43%
57%
38%
62%
42%
58%
40%
60%

634 ~~3.2.3.~~

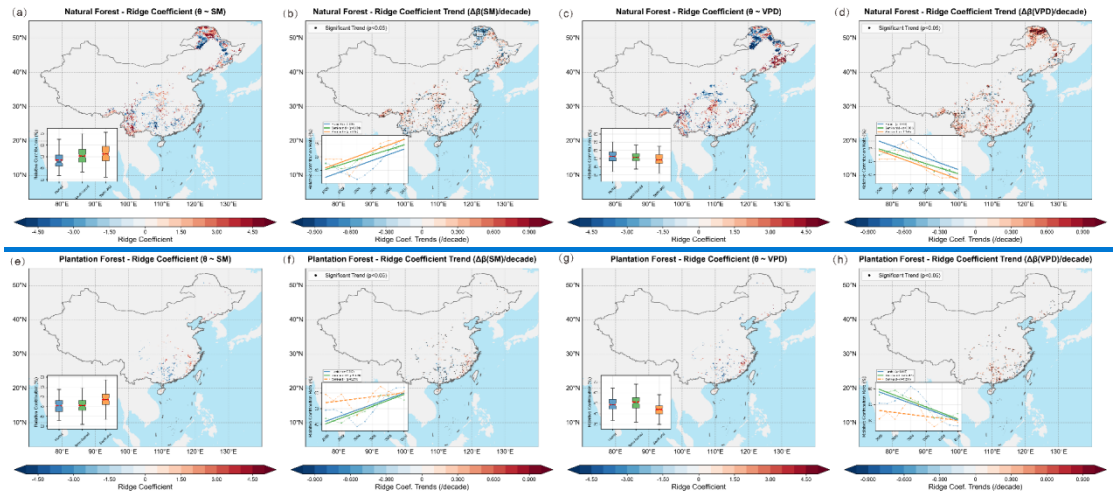

Figure 7. Spatial distribution of ridge-regression standardized coefficients and dominant hydrological driver for forest θ. For natural forests (NF), (a) and (b) show the spatial distributions of β_{SM} and β_{VPD}, respectively, and (c) shows the corresponding dominance pattern. (d)–(f) show the same results for plantation forests (PF). (g) and (i) summarize the zonal means and variability of β_{SM} and β_{VPD} for NF and PF, respectively, and (h) and (j) show the fractions of SM- and VPD-dominated pixels across climatic zones. Warm colors indicate positive coefficients and cool colors indicate negative coefficients; blue and red in dominance maps denote SM-dominated and VPD-dominated pixels, respectively. ~~**Figure 6 Ridge regression coefficients of forest LAI-TF sensitivity (θ) with SM/VPD and their decadal trends. (a–d for NF, e–h for PF).** (a, e) and (c, g) show the spatial distribution of standardized ridge regression coefficients for SM (β_{SM}) and VPD (β_{VPD}), respectively. These coefficients, based on 1995–2015 time series, indicate the independent contribution strength of each factor to θ changes. Inset plots are boxplots of coefficient values for each climatic zone (Humid, Semi-humid, Semi-arid). (b, f) and (d, h) show the temporal trends (decade^{-1}) of β_{SM} and β_{VPD}, respectively. These trends are from Theil-Sen slope estimation and Mann-Kendall tests on the time series of coefficients calculated per-pixel, per-sliding-window. Black dots indicate significant trends (p~~

~~< 0.05). Inset plots show temporal trends of spatially averaged coefficients for each climatic zone (solid for significant, dashed for non-significant).~~

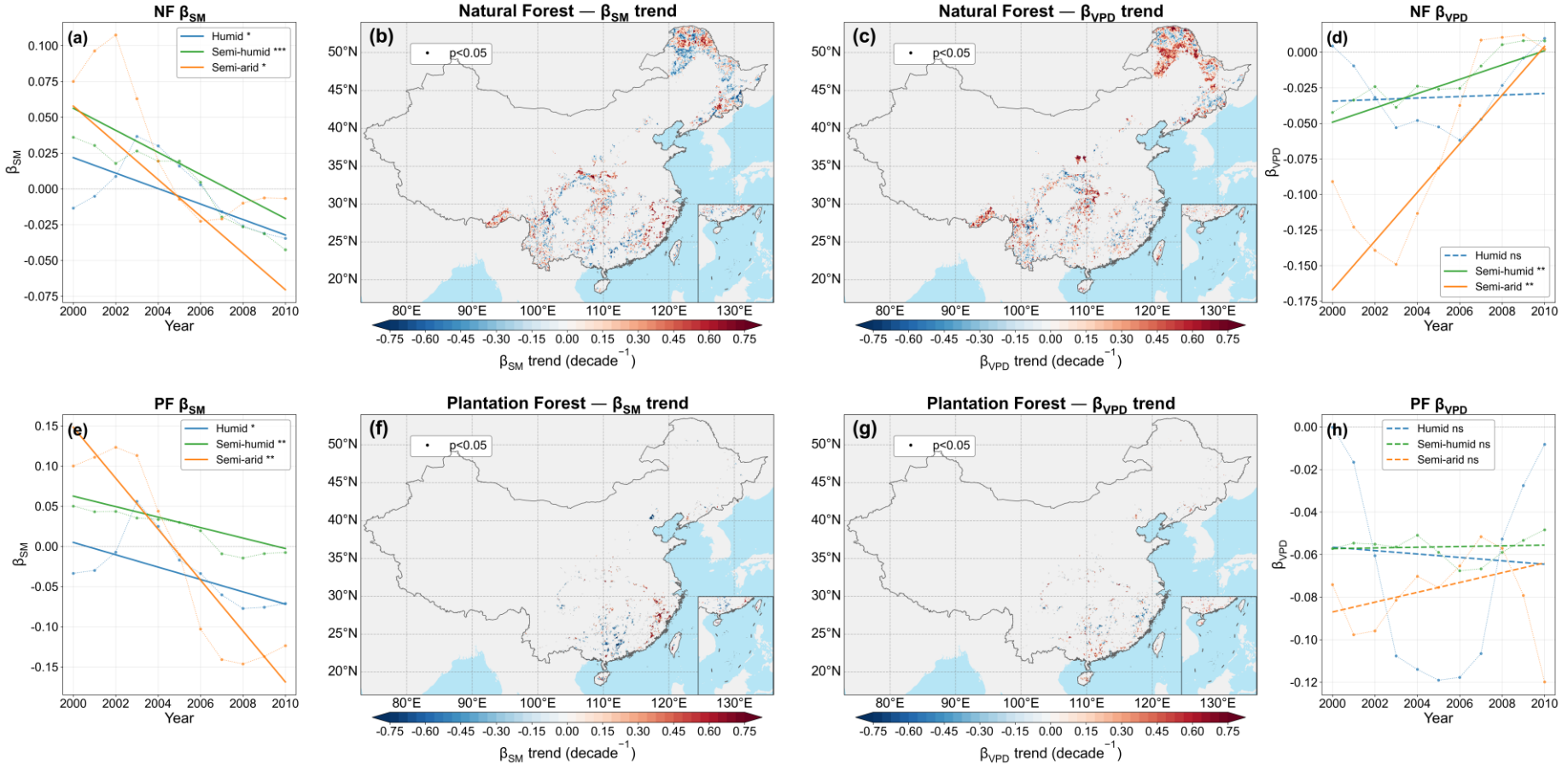

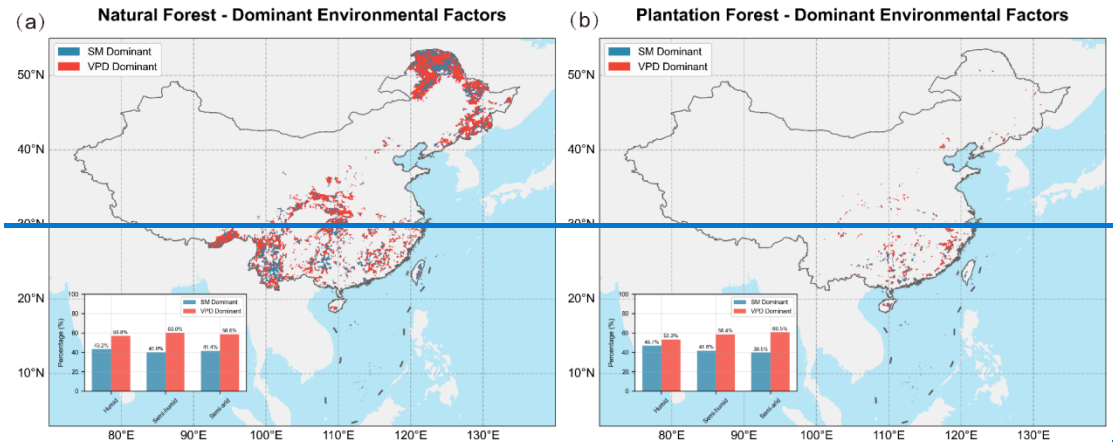

Figure 8. Temporal evolution and spatial trends of ridge-regression coefficients for forest θ (a) and (e) show the temporal evolution of zone-averaged β_{SM} for NF and PF, respectively; (b) and (f) show the corresponding spatial trends in β_{SM}. (d) and (h) show the temporal evolution of zone-averaged β_{VPD} for NF and PF, respectively; (c) and (g) show the corresponding spatial trends in β_{VPD}. Trend slopes were estimated using the Theil–Sen estimator, and significant pixels based on the Mann–Kendall test ($p < 0.05$) are ~~marked~~indicated by black dots. Solid trend lines indicate significant trends, and dashed lines indicate non-significant trends.

~~**Figure 7 Relative contribution rate of SM/VPD to forest LAI-TF sensitivity (θ).** (a) Natural Forest (NF), (b) Planted Forest (PF). For each pixel, the absolute values of ridge regression coefficients are compared: if $|\beta_{SM}| > |\beta_{VPD}|$, it is SM-dominated (blue); otherwise, VPD-dominated (red). Inset bar charts show the percentage of SM/VPD-dominated area in each arid/humid zone.~~

~~The coefficient for SM generally rises, while the coefficient for VPD falls (Δβ(SM)/decade>0, Δβ(VPD)/decade<0), with most regions reaching significance (p<0.05). This "SM↑, VPD↓" direction is consistent across NF, PF, and all three climatic zones, with the change being most pronounced in the semi-arid zone (Fig. 6b,d,f,h inset plots). After determining the dominant factor by relative contribution, VPD-dominant pixels are in the majority nationally, and slightly more so in NF~~

~~than PF: in NF, the SM/VPD dominance ratios for humid/semi-humid/semi-arid zones are 43.2%/56.8%, 40.0%/60.0%, and 41.4%/58.6%, respectively; for PF, they are 46.7%/53.3%, 41.6%/58.4%, and 39.5%/60.5% (Fig. 7). In NF, the VPD coefficient is more "negative" and has greater dispersion (Fig. S3), especially in the semi-arid zone (lower whisker reaching ~ −6), reflecting a stronger and more unstable inhibitory effect of VPD on θ. SM's median is near 0 to slightly negative, with a narrow distribution. In PF, the medians for both factors are slightly negative, but SM's median and upper quartile are generally higher than VPD's, and the upper whisker is higher in the semi-arid zone, suggesting that in relatively arid afforested areas, the positive (or weakening negative) impact of SM on θ is more easily captured. Overall, the spatial explanation of θ is currently dominated by VPD, but over time, SM's relative role is strengthening while VPD's is weakening. This trend is most significant in the semi-arid zone; meanwhile, the proportion of SM dominance in PF is slightly higher than in NF.~~

3.3. ~~A~~Pathway attribution of macro-climate effects on θ ~~ttribution of Macro-climate Change Impacts on θ~~

Pathway analysis ~~suggested~~indicated that the effects of macroclimate change on θ –varied strongly among drivers, climatic zones, and forest types (Figure 9). In natural forests (NF), precipitation generally showed negative direct effects, especially in the semi-humid and semi-arid zones, while its indirect effects differed among pathways, including positive VPD-mediated effects in humid and semi-arid zones. Temperature was the most consistent negative direct driver in NF, with particularly strong negative effects in humid and semi-arid regions, while its indirect effects differed ~~by~~ according to pathway, including positive VPD-mediated effects in humid and semi-arid zones. In plantation forests (PF), the pathway structure was more heterogeneous~~:~~; specifically, precipitation showed a significant positive direct effect in the semi-arid zone, temperature showed opposite indirect effects through SM and VPD in the humid zone, and net radiation and wind speed mainly exerted pathway-specific effects in humid ~~or~~ and semi-humid regions. Overall, the pathway coefficients indicated strong dependence on hydroclimatic context and forest type in how macroclimate trends were associated with changes in θ, with no single pathway dominating across all climate drivers and zones. A supplementary mediator-specification comparison showed that the direction of VPD-mediated indirect effects was generally more robust across single-mediator and joint models than that of SM-mediated effects, whereas SM-mediated pathways were more sensitive to model specification under SM–VPD coupling (Figure S19).

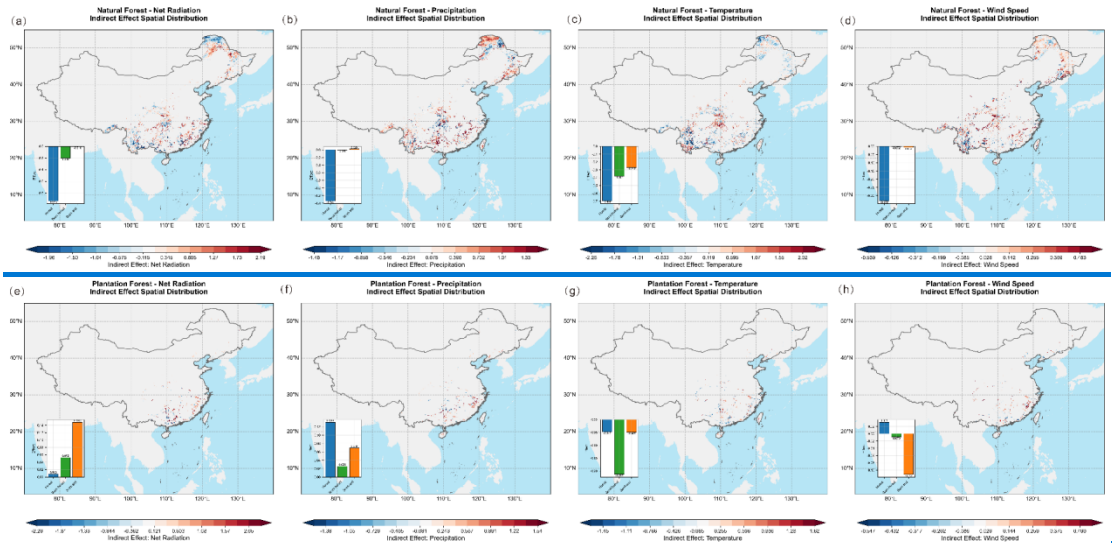

~~**Figure 8** Mediation effects of climate change on forest transpiration sensitivity (θ) via hydrological~~

processes. Natural Forest (NF) and Planted Forest (PF). Spatial distribution of indirect effects from macro-climate factors (Radiation, Precipitation, Temperature, Wind Speed) on θ sensitivity in NF (a–d) and PF (e–h), mediated by local water conditions (SM and VPD). Red (positive) indicates climate change enhances θ via hydrological processes; blue (negative) indicates weakening. Inset plots show the mean indirect effect values for each climatic zone (Humid, Semi-humid, Semi-arid).

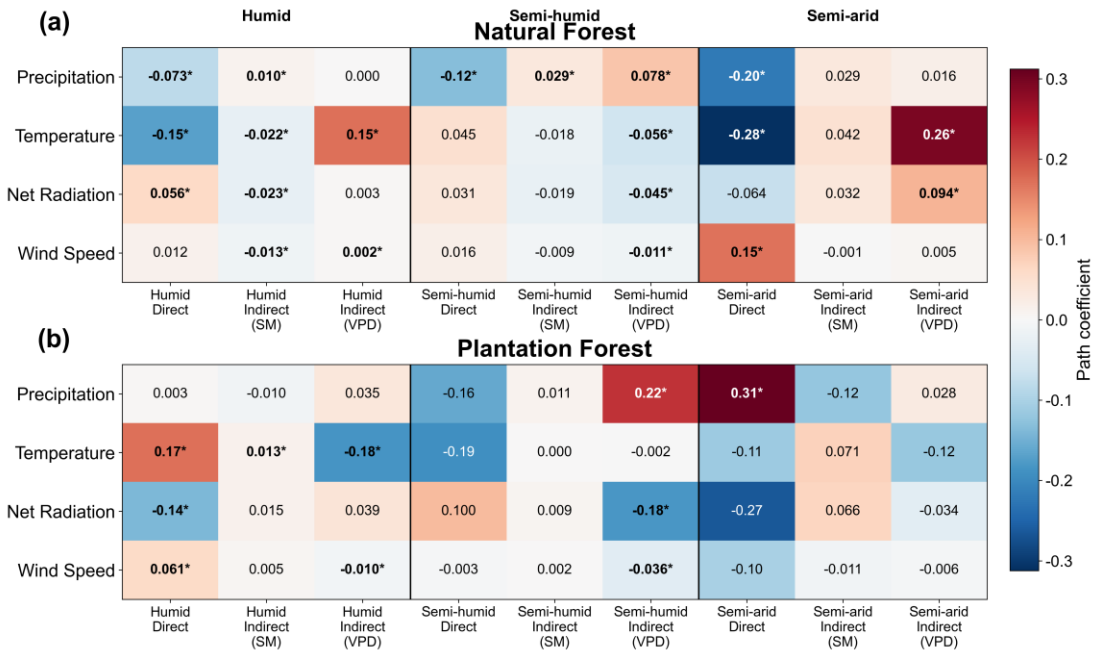

To explore the indirect impact of macro-climate factors on θ, we used a mediation effect model to decompose the transmission pathways of climate change via local hydrological processes (SM and VPD). The model's explanatory power (R^2) for θ was 0.39 for NF and 0.35 for PF. Overall, the total indirect effect of climate change on θ was a weak net negative for both NF (mean −0.0163) and PF (mean −0.0125), mainly resulting from the mutual cancellation of stronger, opposing indirect effects from different climate factors. The specific indirect effects of each climate factor show significant spatial heterogeneity, path dependence, and forest type differences (Fig. 8, Fig. 9): Ta is the most consistent negative driver, exerting a negative effect on both forest types in almost all zones, and much stronger in NF (total effect -0.27 to -0.70) than in PF (total effect -0.04 to -0.21). P shows the strongest type differentiation: for PF, P has a positive promotional effect in all zones (total effect +0.02 to +0.13); but for NF, P shows an extremely strong negative inhibition in the humid zone (total effect -1.34), turning slightly positive in the semi-arid zone (+0.02). Rn also shows type

~~differentiation, with a negative effect on NF (especially in the humid zone, total effect -0.93), but a positive effect on PF (especially in the semi-arid zone, total effect +0.14). WS's indirect effect is weakest overall, mainly showing a slight negative effect in the NF humid zone (-0.33) and the PF semi-arid zone (-0.11). Path decomposition (Fig. 9 and detailed data) further reveals the transmission mechanisms: contrary to the initial hypothesis, in the NF humid zone where effects are strongest, the SM path is absolutely dominant. The indirect effects of P (-1.49), Ta (-0.50), Rn (-0.96), and WS (-0.26) are all primarily transmitted via the SM path, while the VPD path effect is relatively weak. The VPD path's dominance is mainly seen in the semi-humid and semi-arid zones; for example, in the NF semi-humid zone, the negative effects of Ta (-0.29) and Rn (-0.24) are contributed mainly by the VPD path. PF's paths are clearer: the positive effects of P and Rn are realized almost entirely through the SM path, while the negative effects of Ta and WS are evident on both SM and VPD paths. Type comparison shows that NF's indirect response to climate drivers (both positive and negative) is much stronger in magnitude than PF's (especially in the humid zone), with the negative effect difference induced by Ta via the VPD path (e.g., semi-humid zone: NF -0.29 vs PF -0.08) being particularly prominent.~~

Figure 9. Heatmap of pathway coefficients across climate zones for natural and plantation

forests. Standardized path coefficients ~~decompose~~ show the decomposition of the effects of four macroclimate drivers (~~Precipitation, Temperature, Net Radiation, and Wind Speed~~ precipitation, temperature, net radiation, and wind speed) on θ_{total} trends into direct effects and indirect effects mediated ~~through~~by SM and VPD for natural forests (a) and plantation forests (b). Rows ~~represent~~ correspond to the four macro-climate drivers, ~~and~~ while columns are grouped by climate zone (~~Humid, Semi-humid, and Semi-arid~~ humid, semi-humid, and semi-arid), each subdivided into direct effects, indirect effects via SM, and indirect effects via VPD. Cell values are standardized coefficients from parallel dual-mediation pathway analysis, and asterisks indicate significance at the 95% level (i.e., bootstrap confidence interval excludes zero). Warm colors ~~denote~~ indicate positive effects, while ~~and~~ cool colors ~~denote~~ indicate negative effects.

~~**Figure 9 Decomposition of indirect effects from Precipitation, Temperature, Radiation, and Wind Speed on θ in Natural Forests (green) and Planted Forests (brown) via Soil Moisture (SM, solid) and Atmospheric Drought (VPD, hatched) pathways in different climatic zones.**~~

4. Discussion

4.1. ~~Nonlinear Response Characteristics of θ~~Nonlinear hydroclimatic regulation of θ

The joint SM–VPD analysis shows that θ was highest under intermediate SM and moderate-to-high VPD, corresponding to relatively strong atmospheric demand, and declined toward both wetter/low-demand and drier/high-demand conditions (Figure 4; Figures S14–S15). This pattern indicates that increased leaf area enhances TF most effectively when water supply is sufficient but not excessive and evaporative demand is strong enough to sustain canopy transpiration. Once soil water becomes limiting or atmospheric demand becomes too strong, stomatal regulation increasingly constrains transpiration to avoid hydraulic damage, so the marginal gain in transpiration per unit increase in LAI declines (Novick et al., 2016; Grossiord et al., 2020; McDowell et al., 2022). Under wetter and weak-demand conditions, the capacity of additional leaf area to increase TF is also reduced because energy limitations, weaker canopy–atmosphere coupling, and larger non-transpirational evaporation fractions all weaken the translation of additional leaf area into transpiration (Konings et al., 2017; Stoy et al., 2019). The supplementary θ diagnostics further suggest that this nonlinearity cannot be explained solely as a bounded geometric effect of TF; part

of the long-term change also reflects shifts in the LAI–TF relationship itself (Figures S6–S13).

~~We found that θ exhibits a significant nonlinear response to the joint SM and VPD gradient, showing a "hump-shaped" pattern nationally (amplified in the middle, attenuated at the extremes), with similar findings on the Tibetan Plateau grasslands (Jin et al., 2023). θ reaches its maximum when SM is at a moderate level and VPD is medium-high; conversely, under extremely humid (high SM, low VPD) or extremely arid (low SM, or super-high VPD) conditions, θ declines significantly (see Fig. 4; Fig. S8, S9). This implies that increasing LAI is most effective at increasing TF in an environment of moderate water supply and evaporative demand (Novick et al., 2016). This nonlinear pattern is highly consistent with plant physiological responses to water supply and atmospheric demand (Liu et al., 2020).~~

~~On one hand, at moderate soil water content with some atmospheric drought pressure, vegetation has both sufficient water for transpiration and high atmospheric demand to drive it (Konings et al., 2017). At this "matching" point, the plant hydraulic system is within its safety margin, and stomatal regulation primarily optimizes carbon gain (Sperry et al., 2017), resulting in a high θ.~~

~~On the other hand, when the environment deviates from this optimal range, rigid constraints appear, causing θ to decline. When soil is dry or VPD is too high, plants limit water loss via stomatal regulation to avoid sharp declines in water potential, which can lead to xylem embolism and hydraulic failure (McDowell et al., 2022; Sperry et al., 2017). The typical stomatal response to high VPD is partial closure, causing the transpiration rate per unit leaf area to show a nonlinear trend of increasing, then leveling off, or even decreasing at high VPD (Grossiord et al., 2020). This means that even if LAI increases, transpiration rates can hardly increase further under extreme atmospheric drought (Yuan et al., 2019). While rising VPD can promote transpiration within a certain range, stomata begin to close beyond a threshold to reduce excessive water loss, leading to simultaneous suppression of transpiration and photosynthesis (Grossiord et al., 2020). In humid conditions, vegetation transpiration is limited by energy supply and the air's diffusion capacity (i.e., system-atmosphere decoupling) (Konings et al., 2017; Zhou and Yu, 2025). Here, additional leaf area struggles to significantly increase transpiration due to light limitation, poor soil aeration, etc. At the same time, rainfall increases the proportion of Ei and Es (Stoy et al., 2019), which also leads to a~~

~~decline in TF.~~

4.2. ~~Long-term Declining Trend of θ~~Long-term weakening of the LAI enhancement effect on TF

The widespread decline in θ, especially across semi-humid to semi-arid transition zones, indicates that the capacity of increasing LAI to enhance TF has weakened over the last three decades (Figure 3). This trend is consistent with a background of warming, rising VPD, and increasing frequency of soil moisture limitation, all of which reduce the effective transpiration response of forests to additional canopy development (Yuan et al., 2019; Lian et al., 2020; Denissen et al., 2022). Rising atmospheric CO_2 may also have contributed to this decline by lowering stomatal conductance and increasing intrinsic water-use efficiency, thereby reducing transpiration demand per unit leaf area even where greening continued (Keenan et al., 2013; Keenan et al., 2016; Lavergne et al., 2019; Liang et al., 2023). At the same time, the supplementary analyses are more consistent with interpreting CO_2 as a temporally coherent background forcing rather than a spatially heterogeneous driver of θ across China's forests (Figure S17; Table S1). Stand development may likewise have modulated this trajectory. Age-related changes in stand structure, rooting depth, canopy roughness, and interception can shift the partitioning of evapotranspiration between transpiration and non-transpirational components, and therefore alter the LAI–TF relationship even without large changes in total leaf area (Fan et al., 2017; Forrester, 2015). However, the age-stratified results show that the higher θ in NF than in PF persisted across age groups, and including stand age did not overturn the broad interpretation of the relative roles of SM and VPD, although the magnitude of change was heterogeneous across forest types and climatic zones (Figure S18; Table S2). Together, these results suggest that CO_2 rise and stand development may act as background modifiers of θ, while the dominant large-scale patterns remain primarily associated with hydroclimatic variability.~~Over the past three decades, θ has shown a significant long-term declining trend (Fig. 3), especially prominent in the semi-arid to semi-humid transition zones. This is consistent with the concurrent meteorological background of rising temperature and VPD, and spatiotemporal redistribution of precipitation and soil moisture (Fig. S5–S7). The "pulling effect" of vegetation greening on TF has generally weakened in recent decades, suggesting a shift in vegetation-water coupling towards a more "water-saving" or "conservative" water-use strategy (Lian et al., 2020). Persistently rising~~

~~atmospheric CO_2 concentrations have increased plant photosynthetic water use efficiency (iWUE) via the "CO_2 fertilization effect" (Keenan et al., 2016, 2013). Over the past 20+ years, the intrinsic iWUE of temperate and boreal forests in the Northern Hemisphere has significantly increased (Lavergne et al., 2019). This increase is primarily attributed to the partial stomatal closure effect caused by rising CO_2 (Liang et al., 2023; Weiwei et al., 2018). To maintain stable internal CO_2 concentrations, stomata reduce their aperture in high-CO_2 environments, thus lowering water loss per unit leaf area (Keenan et al., 2013). Therefore, vegetation at the same LAI today may support higher photosynthetic carbon assimilation with less transpiration, meaning the transpiration demand per unit leaf area has decreased. This directly leads to a declining trend in θ – because increasing leaf area no longer translates into proportionally higher transpiration rates as it did in the past. This indicates vegetation's water use has become more conservative.~~

~~Atmospheric aridification (VPD rise) has shown a global surge since the late 1990s (Grossiord et al., 2020; Yuan et al., 2019). This is due to rising temperatures increasing saturation vapor pressure, while insufficient continental actual vapor supply leads to decreased relative humidity (Yuan et al., 2019). The atmosphere has become drier, and plants more frequently encounter high VPD stress, forcing them into longer periods of stomatal closure or partial closure to avoid transpiration-induced water deficits (Grossiord et al., 2020; Y. Liu et al., 2020). High VPD not only directly suppresses photosynthesis and transpiration rates but has also been found to slow vegetation growth in many regions (Yuan et al., 2019). Yuan et al. (2019) pointed out that the global vegetation "greening" trend slowed significantly after 1998, primarily because the sharp rise in VPD offset the potential promotional effects of CO_2 fertilization. Even if LAI continues to increase, water stress induced by atmospheric drought will limit the transpiration function of additional leaf area, thereby reducing θ. Jin et al. (2023) noted that as the climate turned drier and VPD rose, the amplifying effect of LAI on TF in Tibetan Plateau grasslands significantly weakened, i.e., θ declined over time; θ did not recover even as drought stress continued to intensify. This is consistent with the significant negative trend we identified in the northern semi-arid to semi-humid transition zone (Fig. 3).~~

4.3. ~~Dynamic Shift of Controlling Factors~~Temporal changes in ~~the hydroclimatic controls~~hydroclimatic effects on θ

Partial correlation, ridge regression, and pathway analysis consistently indicate that the

hydroclimatic controls on θ have changed over time, with the relative role of SM strengthening and that of VPD weakening in many regions (Figures 5–9). This does not mean that atmospheric demand has ceased to matter; VPD still explains a slightly larger share of the present spatial pattern of θ, as also supported by the dominance statistics and multicollinearity diagnostics (Figure 7; Figure S16). The more important point is that the sensitivity of θ to soil moisture limitation has intensified under recent climatic conditions. This interpretation is physically consistent with the increasing prevalence of water-limited ecosystem behavior under warming, in which rising evaporative demand is increasingly translated into ecological stress through soil-water depletion rather than through atmospheric forcing alone (Berg et al., 2016; Denissen et al., 2022). Once ecosystems approach critical soil-moisture thresholds more frequently, stomatal and hydraulic regulation become more tightly constrained by water supply, and the explanatory role of SM rises accordingly (Fu et al., 2022; Liu et al., 2025). The pathway results add the same message at a broader scale: temperature exerted generally negative effects on θ, whereas the effects of precipitation and radiation varied by forest type and climatic zone, implying that macroclimate trends influence θ through multiple hydroclimatic pathways rather than through a single dominant mechanism.~~uniformlydeffects s of SM and VPD strengthening and weakening, respectively,acrossuresHowever, thishave an impactindeed, analysis perhaps consistent with the physical mechanisms associated with the has been as a consequence of VPDAs SM thus support conclusion n even; specifically,generally indicating impact Our multi-evidence diagnosis (ridge regression, partial correlation, and mediation path analysis) jointly reveals that during 1990–2020, the key environmental factors controlling θ underwent a gradual shift from the "demand-side" (VPD) to the "supply-side" (SM). Temporally, Fig. 6 shows β_{SM} rising and β_{VPD} falling. Spatially, the partial correlation trends in Fig. 5 also indicate that the negative constraint of r(θ, SM | VPD) is strengthening in most humid and semi-humid pixels, while the negative constraint of r(θ, VPD | SM) is weakening. This "SM constraint strengthening – VPD constraint relatively weakening" evolution does not mean VPD is no longer important. Spatially, VPD-dominated areas are still more widespread (Fig. 7), but under the same background, SM's marginal control on θ is rising. This shift in dominant factors aligns with the macro-context of water supply-demand pattern reshaping under global warming: more regions are transitioning from energy-limited to water-limited (Berg et al., 2016; Denissen et al., 2022), and~~

~~ecosystem functions are increasingly constrained by soil available water. This widespread shift from energy to water limitation will continue in both time and space, thereby systematically increasing SM's explanatory power for ecosystem transpiration and related processes (Zhou et al., 2019), which is consistent with the signal we captured from θ's temporal change.~~

~~The physical picture of this driver shift can be attributed to the dual role of climate warming on the land water cycle. Continuous warming raises saturation vapor pressure and pushes up VPD, increasing potential transpiration demand (Novick et al., 2016; Yuan et al., 2019). However, in the dual environment of high CO_2 and high VPD, vegetation suppresses transpiration through stomatal conservatism and hydraulic risk aversion (Grossiord et al., 2020; McDowell et al., 2022), leading to a decrease in VPD's marginal drive on θ (i.e., β_{VPD} and r(θ,VPD|SM) weaken). At the same time, the intra-annual/inter-annual redistribution and extremization of precipitation (Fig. S6), coupled with rising Rn and Ta (Fig. S5, S7), cause more regions to cross critical soil moisture thresholds more frequently, entering a water-limited state (Fu et al., 2022; Xu et al., 2019). Once this threshold is crossed, stomatal regulation becomes conservative, VPD's marginal drive is "locked" (Liu et al., 2025), and SM becomes the dominant constraint on θ (Hirschi et al., 2025; Liu et al., 2025). This corresponds exactly to the rising β_{SM} we see in Fig. 6 and the significant downward trend of r(θ, SM|VPD) (negative correlation strengthening) over time in Fig. 5.~~

~~From 1990-2020, the rise in β_{SM} and fall in β_{VPD} is a widespread signal, but in terms of spatial extent, VPD-dominant pixels still form the majority – especially in semi-arid/transition zones. This conclusion of a "shift in intensity rather than a replacement of spatial dominance" is consistent with the latest multi-modal evidence: warming continuously increases the *ability* to need water (atmospheric dryness), but the *ability* to access water (effective soil water) is more quickly becoming the bottleneck for E/T (Berg et al., 2016; IPCC, 2023). The result is that θ's elasticity to SM increases, while its independent elasticity to VPD decreases. This is mutually supported by our three sets of evidence from ridge regression, partial correlation, and mediation effects.~~

4.4. Contrasting ecohydrological responses of natural and plantation forests~~Differences in Response Mechanisms between NF and PF~~

The contrast between natural and plantation forests remained one of the clearest features of the analysis. NF consistently showed higher θ, and high-θ values in NF were maintained across a wider

range of SM–VPD backgrounds, whereas PF showed lower θ and a more restricted range of hydroclimatic conditions under which high θ occurred. This pattern likely reflects differences between long-term spatial hydroclimatic contrasts and within-pixel temporal variability. Spatial contrasts integrate longer-term differences in stand structure, species composition, hydraulic diversity, and belowground water access, whereas temporal anomalies are expressed more directly through canopy–atmosphere coupling and stomatal–hydraulic regulation during drought (Martínez-Vilalta & García-Forner, 2017; Grossiord et al., 2020; Novick et al., 2024; Bachofen et al., 2024). Under this interpretation, the broader hydroclimatic response of NF may reflect the greater structural and functional heterogeneity often associated with natural forests, while the narrower response of PF may reflect the relative structural simplification typical of many plantation stands. This interpretation is also consistent with evidence that higher hydraulic diversity can buffer ecosystem drought responses (Anderegg et al., 2018).~~NF and PF results outcomes ; in contrast,values values were observedmore directly associated withsuch an would NFwould most previous research indicating~~ The age-stratified supplementary results are consistent with this interpretation, because the higher θ in NF than in PF persisted across age classes and this pattern is therefore unlikely to be explained solely by stand age.~~asvalues in NF than in PF persisted across age classes and are NF's θ is generally higher, more sensitive to VPD's independent inhibition, and has greater dispersion, while PF's θ has a lower base value, declines faster, and its interannual variability and spatial patterns are more significantly controlled by SM's marginal effect. This differentiation stems first from fundamental differences in community structure and hydraulic strategies. NF is composed of multiple species, ages, and canopy layers, possessing greater hydraulic and trait diversity (Anderegg et al., 2018), including different isohydric/anisohydric control strategies (Martínez-Vilalta and Garcia-Forner, 2017), vulnerability to embolism, and deep-shallow root complementarity (Zhang et al., 2025). NF's structure, on one hand, provides resilience to drought disturbances (Anderegg et al., 2018), and on the other, leads to a stronger stomatal conservative response during high VPD (Grossiord et al., 2020). This manifests in our ridge regression and partial correlations as a larger β_{VPD}, a more negative and dispersed r(θ, VPD|SM) (Fig. 6, Fig. S3), and a relatively flat independent correlation with SM (Fig. 5). Conversely, PF is mostly even-aged, with single or few fast-growing species, simple canopy structure, predominantly shallow roots, and converged~~

hydraulic traits (Farley et al., 2005). This leads to a more significant "synchronous resonance" of community transpiration during surface soil water fluctuations—thus, the negative constraint of r(θ, SM|VPD) is stronger and its decadal strengthening is more prevalent (Fig. 5b, 5f), and the rise in β_{SM} is also more pronounced (Fig. 6f, 6h). This is perfectly consistent with the differences in the nonlinear "peak in the middle, attenuated at the ends" response window we see in Fig. 4: NF's "usable window" is wider (regions of moderate SM × medium-high VPD can better convert LAI increases into TF increases), while PF's window is narrower and attenuates earlier at the extremes (extremely wet or dry, extremely high VPD), indicating its hydraulic safety margin is smaller and it is more sensitive to supply-side deficits (McDowell et al., 2022).

Mediation analysis tells us "who affects θ via which path" (Fig 8–9). In NF humid zones, the negative indirect effects of P, Ta, Rn, and WS on θ are almost all transmitted via the SM path, while the VPD path is relatively minor or opposite in direction. This, on one hand, reflects that under thick canopy conditions, changes in P and Rn more easily amplify canopy interception and soil evaporation, thus "diluting" TF (Chen et al., 2022). On the other hand, it also shows that the combined effect of deep roots, roughness, and litter layer in humid zone NF makes the community insensitive to transient SM deficits, but more sensitive to "energy-turbulence limitation" caused by prolonged wet SM (Huang et al., 2025). In contrast, PF in most zones shows positive indirect effects from P and Rn primarily through the SM path, meaning that once soil water supply improves or canopy transpiration potential is released by increased radiation, PF can quickly convert LAI increases into TF increases; but in phases of negative SM, its θ also decays faster. This runs parallel to the national trend of rising β_{SM} and falling β_{VPD}: spatially, both forest types still have a majority of VPD-dominant pixels, but in terms of intensity, SM's marginal constraint is rising synchronously, and the proportion of SM-dominated area in PF is slightly higher, which aligns perfectly with the "one strengthens, one weakens" partial correlation trend.

NF's "VPD-sensitive, SM-buffered" combination fits its deep-root acquisition and hydraulic diversity (Fan et al., 2017; Zhang et al., 2025): deep roots enhance coupling with groundwater or deep soil water reservoirs, reducing exposure to surface SM fluctuations. But when atmospheric dryness rises to a threshold (Novick et al., 2016), community-wide stomatal conservatism suppresses the transpiration increment per unit LAI (Grossiord et al., 2020), making θ more elastic

~~(negatively) to VPD. At the same time, the thick canopy and rough surface deepen ensemble layer-atmosphere coupling, making energy/turbulence-limited TF dilution more likely in humid zones (consistent with the "most climate factors → SM path → negative θ effect" in humid zone NF). PF's "SM-sensitive, VPD-relatively-insensitive" stems from its shallow-root, even-aged, trait-convergent nature: any shortage in soil water supply is quickly and synchronously reflected in canopy stomatal conductance and transpiration, causing θ to show a stronger and decadally strengthening negative correlation with SM. In humid situations, once SM and radiation improve, the "rehydration re-energizing" release for TF is more direct, explaining the positive SM-path effects of P and Rn in most PF zones. Therefore, when we overlay "type difference" with "temporal shift," VPD remains the primary dominant factor explaining θ's current pattern, but in terms of intensity, SM's marginal control is rising (Berg et al., 2016); this rise is faster and more significant in PF. This also implies that under a warming-drying background, NF is more likely to be suppressed in high-VPD years (VPD-dominated stomatal conservatism, θ decline), while PF is more likely to decelerate uniformly when supply bottlenecks appear (SM-dominated threshold crossing), causing θ to fall faster.~~

~~Management implications: PF should prioritize enhancing trait and root-depth diversity via mixed-species planting and thinning to reduce synchronous dependence on surface soil water, and configure deeper-rooted or drought-tolerant species in arid-sensitive areas to widen the "effective water window" and reduce threshold-crossing risks (Forrester, 2015). NF should maintain and restore multi-layered canopy structure, roughness, and understory cover to reduce the "dilution" of TF by non-transpiration components (Ei/Es), and alleviate community-scale stomatal stress and hydraulic risk in high-VPD seasons/regions by reducing density to improve ventilation/turbulence coupling. Overall, the conclusion that NF is more constrained by the "atmospheric side" and PF by the "soil side" is consistent with our multi-evidence picture of θ's spatial differentiation, decadal trends, and path decomposition, and provides clear direction for type-based water management in a warming, acidifying background.~~

4.5. Implications and limitations

~~These results imply~~These results imply that further greening will not necessarily translate into proportionally higher transpiration fractions under continued warming and drying. In regions where

hydroclimatic water stress is increasing, especially across semi-humid to semi-arid transition zones, the ecohydrological consequences of increasing canopy leaf area depend increasingly on soil water supply, and this dependence appears more evident in plantation forests than in natural forests. This has direct management implications: plantation design may benefit from greater rooting-depth and trait diversity and from stand structures that reduce rapid soil-water depletion, whereas natural forests may benefit more from maintaining multilayer canopy structure and hydraulic diversity under rising atmospheric demand. Several limitations should remain explicit. A nationwide in situ benchmark for θ trends is not yet available because long-term observations that simultaneously resolve transpiration partitioning, LAI dynamics, and stand development remain too sparse across China's forests. We therefore evaluated robustness through cross-product consistency rather than direct site-based validation. In addition, because θ, SM, and VPD were analyzed from growing-season aggregates and moving-window series, the results characterize seasonal-to-interannual hydroclimatic controls rather than instantaneous stomatal responses to short-lived atmospheric fluctuations. Even with these constraints, the convergence among the main analyses, the supplementary robustness checks, and the CO_2- and age-sensitivity diagnostics supports the central inference that the enhancement of TF by increasing LAI has weakened across China's forests and is increasingly shaped by soil moisture limitation~~The results of the present study indicateresult in TF with persistently increasing hydroclimatic water stresswas exhibitedPF NFfinding ; for example,species selection for NF management for However, several of the present workbe made Development of a nationwide in situ benchmark for θ trends is not yet feasible vast forested areaby assessing Additionallyzeffects termDespite these limitationsconsistency of results analyses to confirm robustness of the results analysescore conclusion TF enhancement caused by increases inhas become SM~~.

5. Conclusion

~~In~~ Across China's forests, the enhancement of ~~transpiration fraction~~ TF ~~by increasing~~ caused by increased LAI has weakened during 1990–2020. VPD still explains a slightly larger share of the present spatial pattern of θ, but the role of SM has strengthened over ~~time~~this timespan, indicating ~~increasing~~ there has been an increase in ~~soil moisture~~SM limitation. Differences between ~~natural and planted forests~~ NF and PF were ~~clear~~obvious: ~~natural forests~~ NF maintained higher θ values,

whereas ~~planted forests~~ PF showed a ~~larger~~ greater long-term decline in θ. ~~Together~~Collectively, these results indicate that continued greening under warming will not necessarily ~~translate into~~ result in proportionally higher ~~transpiration fractions~~TF, particularly in semi-humid to semi-arid transition regions.~~Based on multi-source data from 1990–2020, this study systematically revealed the spatiotemporal differentiation and hydrological driving mechanisms of LAI-TF sensitivity (θ) in China's NF and PF. Overall, θ spatially increases from humid to semi-arid regions (NF > PF) and temporally shows a widespread significant declining trend (PF decline is larger, mean −0.262 %·m^{-2}·m^{2}·decade^{-1}), especially in ecological transition zones, indicating that the enhancing effect of LAI on TF is systematically weakening. Mechanistically, the controlling factors of θ are undergoing a gradual shift from the "atmospheric demand-side" (VPD) to the "soil supply-side" (SM): although VPD remains the spatially dominant factor (coverage > 50%), its independent control has weakened over time, while SM's has significantly strengthened. Forest type differences are significant: NF (θ higher) is "VPD-sensitive, SM-buffered," showing a stronger response to atmospheric drought; PF (θ lower, declining faster) is "SM-sensitive, VPD-insensitive," showing more sensitivity to soil moisture stress. Mediation analysis confirmed that warming is a consistent negative driver of θ decline, while the effects of precipitation and radiation vary by forest type. China's forests are shifting towards a more "conservative" water-use strategy. This finding provides a scientific basis for climate-adaptive forest management (e.g., type-based root optimization and turbulence enhancement).~~

Author contributions

Xiao Zhang performed the analysis, prepared the figures, and drafted the manuscript. Xinxiao Yu contributed to the study design, interpretation of the results, and manuscript revision. Guodong Jia conceived and supervised the study, contributed to the analytical framework, and revised the manuscript. All authors discussed the results and approved the final manuscript.

Competing interests

The authors declare that they have no conflict of interest.

~~Availability of data and materials~~Code and data availability

~~Available on request.~~The datasets used in this study are publicly available from the sources

cited in Table 1. The processed data and code supporting the findings of this study are available from the corresponding author upon reasonable request.

Funding

This research was supported by the National Natural Science Foundation of China (~~Nos.~~ grant numbers 42277062, 41977149, and 42230714).

~~Availability of data and materials~~

~~Available on request.~~

~~Declaration of Competing Interest~~

~~The authors declare that they have no known competing financial interests or personal relationships that could have appeared to influence the work reported in this paper.~~

References

Anderegg, W.R.L., Konings, A.G., Trugman, A.T., Yu, K., Bowling, D.R., Gabbitas, R., Karp, D.S., Pacala, S., Sperry, J.S., Sulman, B.N. and Zenes, N. (2018) Hydraulic diversity of forests regulates ecosystem resilience during drought. *Nature*, 561, 538–541. doi:10.1038/s41586-018-0539-7

Bachofen, C., Tumber-Dávila, S.J., Mackay, D.S., McDowell, N.G., Carminati, A., Klein, T., Stocker, B.D., Mencuccini, M. and Grossiord, C. (2024) Tree water uptake patterns across the globe. *New Phytologist*, 242, 1891–1910. doi:10.1111/nph.19762

Berg, A., Findell, K., Lintner, B., Giannini, A., Seneviratne, S.I., van den Hurk, B., Lorenz, R., Pitman, A.J., Hagemann, S., Meier, A., Cheruy, F., Ducharne, A., Malyshev, S. and Milly, P.C.D. (2016) Land–atmosphere feedbacks amplify aridity increase over land under global warming. *Nature Climate Change*, 6, 869–874. doi:10.1038/nclimate3029

Buck, A.L. (1981) New equations for computing vapor pressure and enhancement factor. *Journal of Applied Meteorology*, 20, 1527–1532. doi:10.1175/1520-0450(1981)020<1527:NEFCVP>2.0.CO;2

Chen, H., Wei, Y. and Huang, J.J. (2024) Widespread increase in plant transpiration driven by global greening. *Global and Planetary Change*, 235, 104395. doi:10.1016/j.gloplacha.2024.104395

Chen, H., Zhu, G., Shang, S., Qin, W., Zhang, Y., Su, Y., Zhang, K., Zhu, Y. and Xu, C. (2022) Uncertainties in partitioning evapotranspiration by two remote sensing-based models. *Journal of Hydrology*, 604, 127223. doi:10.1016/j.jhydrol.2021.127223

Cheng, K., Chen, Y., Xiang, T., Yang, H., Liu, W., Ren, Y., Guan, H., Hu, T., Ma, Q. and Guo, Q. (2024a) A 2020 forest age map for China with 30 m resolution. Earth System Science Data, 16, 803–819. doi:10.5194/essd-16-803-2024.

Cheng, K., Yang, H., Guan, H., Ren, Y., Chen, Y., Chen, M., Yang, Z., Lin, D., Liu, W., Xu, J., Xu, G., Ma, K. and Guo, Q. (2024b) Unveiling China's natural and planted forest spatial–temporal dynamics from 1990 to 2020. *ISPRS Journal of Photogrammetry and Remote Sensing*, 209, 37–50. doi:10.1016/j.isprsjprs.2024.01.024

Cheng, K., Zhang, Y., Yang, H., Ren, Y., Xiang, T., Chen, Y., Yang, Z., Chen, M., Xu, J., Huang, G., Xu, G., Tao, S., Yu, Z. and Guo, Q. (2025) China's naturally regenerated forests currently have greater aboveground carbon accumulation rates than newly planted forests. *Communications Earth & Environment*, 6, 345. doi:10.1038/s43247-025-02323-z

Denissen, J.M.C., Teuling, A.J., Pitman, A.J., Koirala, S., Migliavacca, M., Li, W., Reichstein, M., Winkler, A.J., Zhan, C. and Orth, R. (2022) Widespread shift from ecosystem energy to water limitation with climate change. *Nature Climate Change*, 12, 677–684. doi:10.1038/s41558-022-01403-8

Fan, Y., Miguez-Macho, G., Jobbágy, E.G., Jackson, R.B. and Otero-Casal, C. (2017) Hydrologic regulation of plant rooting depth. *Proceedings of the National Academy of Sciences of the United States of America*, 114, 10572–10577. doi:10.1073/pnas.1712381114

Farley, K.A., Jobbágy, E.G. and Jackson, R.B. (2005) Effects of afforestation on water yield: a global synthesis with implications for policy. *Global Change Biology*, 11, 1565–1576. doi:10.1111/j.1365-2486.2005.01011.x

Farooq, T.H., Shakoor, A., Wu, X., Li, Y., Rashid, M.H.U., Zhang, X., Gilani, M.M., Kumar, U., Chen, X. and Yan, W. (2021) Perspectives of plantation forests in the sustainable forest

development of China. iForest - Biogeosciences and Forestry, 14, 166–174. doi:10.3832/ifor3551-014.

Forrester, D.I. (2015) Transpiration and water-use efficiency in mixed-species forests versus monocultures: effects of tree size, stand density and season. *Tree Physiology*, 35, 289–304. doi:10.1093/treephys/tpv011

Fu, Z., Ciais, P., Feldman, A., Gentine, P., Makowski, D., Prentice, I.C., Stoy, P.C., Bastos, A. and Wigneron, J.-P. (2022) Critical soil moisture thresholds of plant water stress in terrestrial ecosystems. *Science Advances*, 8, eabq7827. doi:10.1126/sciadv.abq7827

Grossiord, C., Buckley, T.N., Cernusak, L.A., Novick, K.A., Poulter, B., Siegwolf, R.T.W., Sperry, J.S. and McDowell, N.G. (2020) Plant responses to rising vapor pressure deficit. *New Phytologist*, 226, 1550–1566. doi:10.1111/nph.16485

Hirschi, M., Stradiotti, P., Crezee, B., Dorigo, W. and Seneviratne, S.I. (2025) Potential of long-term satellite observations and reanalysis products for characterising soil drying: trends and drought events. *Hydrology and Earth System Sciences*, 29, 397–425. doi:10.5194/hess-29-397-2025

Hu, Y., Wei, F., Fu, B. and Zhang, W. (2023) Ecosystems in China have become more sensitive to changes in water demand since 2001. *Communications Earth & Environment*, 4, 444. doi:10.1038/s43247-023-01105-9

Huang, X., Liang, S., Ziegler, A.D. and Zeng, Z. (2025) Decoupling vegetation and soil-moisture interaction in evapotranspiration interannual variability. *iScience*, 28, 113008. doi:10.1016/j.isci.2025.113008

Intergovernmental Panel on Climate Change (IPCC) (2023) Weather and climate extreme events in a changing climate. In: *Climate Change 2021 – The Physical Science Basis: Working Group I Contribution to the Sixth Assessment Report of the Intergovernmental Panel on Climate Change*. Cambridge University Press, Cambridge, pp. 1513–1766. doi:10.1017/9781009157896.013

Jin, Z., You, Q., Zuo, Z., Li, M., Sun, G., Pepin, N. and Wang, L. (2023) Weakening amplification of grassland greening to transpiration fraction of evapotranspiration over the Tibetan Plateau during 2001–2020. *Agricultural and Forest Meteorology*, 341, 109661. doi:10.1016/j.agrformet.2023.109661

Keenan, T.F., Hollinger, D.Y., Bohrer, G., Dragoni, D., Munger, J.W., Schmid, H.P. and Richardson, A.D. (2013) Increase in forest water-use efficiency as atmospheric carbon dioxide concentrations rise. *Nature*, 499, 324–327. doi:10.1038/nature12291

Keenan, T.F., Prentice, I.C., Canadell, J.G., Williams, C.A., Wang, H., Raupach, M. and Collatz, G.J. (2016) Recent pause in the growth rate of atmospheric CO2 due to enhanced terrestrial carbon uptake. *Nature Communications*, 7, 13428. doi:10.1038/ncomms13428

Koehler, T., Wankmüller, F.J.P., Sadok, W. and Carminati, A. (2023) Transpiration response to soil drying versus increasing vapor pressure deficit in crops: physical and physiological

mechanisms and key plant traits. *Journal of Experimental Botany*, 74, 4789–4807. doi:10.1093/jxb/erad235

Konings, A.G., Williams, A.P. and Gentine, P. (2017) Sensitivity of grassland productivity to aridity controlled by stomatal and xylem regulation. *Nature Geoscience*, 10, 284–288. doi:10.1038/ngeo2903

Lavergne, A., Graven, H., De Kauwe, M.G., Keenan, T.F., Medlyn, B.E. and Prentice, I.C. (2019) Observed and modelled historical trends in the water-use efficiency of plants and ecosystems. *Global Change Biology*, 25, 2242–2257. doi:10.1111/gcb.14634

Li, C., Han, J., Liu, Z., Tu, Z. and Yang, H. (2024) A harmonized global gridded transpiration product based on collocation analysis. *Scientific Data*, 11, 604. doi:10.1038/s41597-024-03425-7

Lian, X., Piao, S., Li, L.Z.X., Li, Y., Huntingford, C., Ciais, P., Cescatti, A., Janssens, I.A., Peñuelas, J., Buermann, W., Chen, A., Li, X., Myneni, R.B., Wang, X., Wang, Y., Yang, Y., Zeng, Z., Zhang, Y. and McVicar, T.R. (2020) Summer soil drying exacerbated by earlier spring greening of northern vegetation. *Science Advances*, 6, eaax0255. doi:10.1126/sciadv.aax0255

Liang, X., Wang, D., Ye, Q., Zhang, J., Liu, M., Liu, H., Yu, K., Wang, Y., Hou, E., Zhong, B., Xu, L., Lv, T., Peng, S., Lu, H., Sicard, P., Anav, A. and Ellsworth, D.S. (2023) Stomatal responses of terrestrial plants to global change. *Nature Communications*, 14, 2188. doi:10.1038/s41467-023-37934-7

Liu, L., Gudmundsson, L., Hauser, M., Qin, D., Li, S. and Seneviratne, S.I. (2020) Soil moisture dominates dryness stress on ecosystem production globally. *Nature Communications*, 11, 4892. doi:10.1038/s41467-020-18631-1

Liu, Y., Kumar, M., Katul, G.G., Feng, X. and Konings, A.G. (2020) Plant hydraulics accentuates the effect of atmospheric moisture stress on transpiration. *Nature Climate Change*, 10, 691–695. doi:10.1038/s41558-020-0781-5

Liu, Y., Lin, Z., Wang, Z., Chen, X., Han, P., Wang, B., Wang, Z., Wen, Z., Shi, H., Zhang, Z. and Zhang, W. (2023) Discriminating the impacts of vegetation greening and climate change on the changes in evapotranspiration and transpiration fraction over the Yellow River Basin. *Science of the Total Environment*, 904, 166926. doi:10.1016/j.scitotenv.2023.166926

Liu, Y., Wang, Y., Zhao, Y., Chen, S., Wang, L., Yang, W., Li, X., Li, X., Lei, H., Chang, H. and others (2025) Evapotranspiration stress intensifies with enhanced sensitivity to soil moisture deficits in a rapidly greening China. *Hydrology and Earth System Sciences*, 29, 3379–3404. doi:10.5194/hess-29-3379-2025

Lu, W.W., Yu, X.X., Jia, G., Li, H. and Liu, Z. (2018) Responses of intrinsic water-use efficiency and tree growth to climate change in semi-arid areas of North China. *Scientific Reports*, 8, 308. doi:10.1038/s41598-017-18694-z

Martínez-Vilalta, J. and Garcia-Forner, N. (2017) Water potential regulation, stomatal behaviour and hydraulic transport under drought: deconstructing the iso/anisohydric concept. *Plant, Cell & Environment*, 40, 962–976. doi:10.1111/pce.12846

McDowell, N.G., Sapes, G., Pivovaroff, A., Adams, H.D., Allen, C.D., Anderegg, W.R.L., Arend, M., Breshears, D.D., Brodribb, T., Choat, B., Cochard, H., De Cáceres, M., De Kauwe, M.G., Grossiord, C., Hammond, W.M., Hartmann, H., Hoch, G., Kahmen, A., Klein, T., Mackay, D.S., Mantova, M., Martínez-Vilalta, J., Medlyn, B.E., Mencuccini, M., Nardini, A., Oliveira, R.S., Sala, A., Tissue, D.T., Torres-Ruiz, J.M., Trowbridge, A.M., Trugman, A.T., Wiley, E. and Xu, C. (2022)

Mechanisms of woody-plant mortality under rising drought, CO2 and vapour pressure deficit. *Nature Reviews Earth & Environment*, 3, 294–308. doi:10.1038/s43017-022-00272-1

Niu, Z., He, H., Zhu, G., Ren, X., Zhang, L. and Zhang, K. (2020) A spatial-temporal continuous dataset of the transpiration to evapotranspiration ratio in China from 1981–2015. *Scientific Data*, 7, 369. doi:10.1038/s41597-020-00693-x

Novick, K.A., Ficklin, D.L., Grossiord, C., Konings, A.G., Martínez-Vilalta, J., Sadok, W., Trugman, A.T., Williams, A.P., Wright, A.J., Abatzoglou, J.T., Dannenberg, M.P., Gentine, P., Guan, K., Johnston, M.R., Lowman, L.E.L., Moore, D.J.P. and McDowell, N.G. (2024) The impacts of rising vapour pressure deficit in natural and managed ecosystems. *Plant, Cell & Environment*, 47, 3561–3589. doi:10.1111/pce.14846

Novick, K.A., Ficklin, D.L., Stoy, P.C., Williams, C.A., Bohrer, G., Oishi, A.C., Papuga, S.A., Blanken, P.D., Noormets, A., Sulman, B.N., Scott, R.L., Wang, L. and Phillips, R.P. (2016) The increasing importance of atmospheric demand for ecosystem water and carbon fluxes. *Nature Climate Change*, 6, 1023–1027. doi:10.1038/nclimate3114

Qing, Y., Wang, S., Ancell, B.C. and Yang, Z.-L. (2022) Accelerating flash droughts induced by the joint influence of soil moisture depletion and atmospheric aridity. *Nature Communications*, 13, 1139. doi:10.1038/s41467-022-28752-4

Schlesinger, W.H. and Jasechko, S. (2014) Transpiration in the global water cycle. *Agricultural and Forest Meteorology*, 189–190, 115–117. doi:10.1016/j.agrformet.2014.01.011

Song, J., Zhou, S., Yu, B., Li, Y., Liu, Y., Yao, Y., Wang, S. and Fu, B. (2024) Serious underestimation of reduced carbon uptake due to vegetation compound droughts. *npj Climate and Atmospheric Science*, 7, 23. doi:10.1038/s41612-024-00571-y

Sperry, J.S., Venturas, M.D., Anderegg, W.R.L., Mencuccini, M., Mackay, D.S., Wang, Y. and Love, D.M. (2017) Predicting stomatal responses to the environment from the optimization of photosynthetic gain and hydraulic cost. *Plant, Cell & Environment*, 40, 816–830. doi:10.1111/pce.12852

Stoy, P.C., El-Madany, T.S., Fisher, J.B., Gentine, P., Gerken, T., Good, S.P., Klosterhalfen, A., Liu, S., Miralles, D.G., Perez-Priego, O., Rigden, A.J., Skaggs, T.H., Wohlfahrt, G., Anderson, R.G., Coenders-Gerrits, A.M.J., Jung, M., Maes, W.H., Mammarella, I., Mauder, M., Migliavacca, M., Nelson, J.A., Poyatos, R., Reichstein, M., Scott, R.L. and Wolf, S. (2019) Reviews and syntheses: turning the challenges of partitioning ecosystem evaporation and transpiration into opportunities. *Biogeosciences*, 16, 3747–3775. doi:10.5194/bg-16-3747-2019

Sun, S., Liu, Y., Chen, H., Ju, W., Xu, C.-Y., Liu, Y., Zhou, B., Zhou, Y., Zhou, Y. and Yu, M. (2022) Causes for the increases in both evapotranspiration and water yield over vegetated

mainland China during the last two decades. *Agricultural and Forest Meteorology*, 324, 109118. doi:10.1016/j.agrformet.2022.109118

Wei, Z., Yoshimura, K., Wang, L., Miralles, D.G., Jasechko, S. and Lee, X. (2017) Revisiting the contribution of transpiration to global terrestrial evapotranspiration. *Geophysical Research Letters*, 44, 2792–2801. doi:10.1002/2016GL072235

Xu, H., Yue, C., Zhang, Y., Liu, D. and Piao, S. (2023) Forestation at the right time with the right species can generate persistent carbon benefits in China. *Proceedings of the National Academy of Sciences of the United States of America*, 120, e2304988120. doi:10.1073/pnas.2304988120

Xu, L., Chen, N. and Zhang, X. (2019) Global drought trends under 1.5 and 2 °C warming. *International Journal of Climatology*, 39, 2375–2385. doi:10.1002/joc.5958

Yuan, W., Zheng, Y., Piao, S., Ciais, P., Lombardozzi, D., Wang, Y., Ryu, Y., Chen, G., Dong, W., Hu, Z., Jain, A.K., Jiang, C., Kato, E., Li, S., Lienert, S., Liu, S., Nabel, J.E.M.S., Qin, Z., Quine, T., Sitch, S., Smith, W.K., Wang, F., Wu, C., Xiao, Z. and Yang, S. (2019) Increased atmospheric vapor pressure deficit reduces global vegetation growth. *Science Advances*, 5, eaax1396. doi:10.1126/sciadv.aax1396

Zahra, N., Hafeez, M.B., Kausar, A., Al Zeidi, M., Asekova, S., Siddique, K.H.M. and Farooq, M. (2023) Plant photosynthetic responses under drought stress: effects and management. *Journal of Agronomy and Crop Science*, 209, 651–672. doi:10.1111/jac.12652

Zhang, J., Liu, N., Zhang, C., Zhang, X., He, X., Jiang, W., Li, J., Zhan, Z., Peng, D., Lv, D. and Ni, S. (2025) Deep soil moisture has limited impact on mitigating drought stress effects on plant transpiration in a subtropical secondary forest. *Plant and Soil*, 514, 427–444. doi:10.1007/s11104-025-07398-3

Zhang, K., Chen, H., Ma, N., Shang, S., Wang, Y., Xu, Q. and Zhu, G. (2024) A global dataset of terrestrial evapotranspiration and soil moisture dynamics from 1982 to 2020. *Scientific Data*, 11, 445. doi:10.1038/s41597-024-03271-7

Zhou, S. and Yu, B. (2025) Neglecting land–atmosphere feedbacks overestimates climate-driven increases in evapotranspiration. *Nature Climate Change*, 15, 1099–1106. doi:10.1038/s41558-025-02428-5

Zhou, S., Zhang, Y., Williams, A.P. and Gentine, P. (2019) Projected increases in intensity, frequency, and terrestrial carbon costs of compound drought and aridity events. *Science Advances*, 5, eaau5740. doi:10.1126/sciadv.aau5740

~~Anderegg, W.R.L., Konings, A.G., Trugman, A.T., Yu, K., Bowling, D.R., Gabbitas, R., Karp, D.S., Pacala, S., Sperry, J.S., Sulman, B.N., Zenes, N., 2018. Hydraulic diversity of forests regulates ecosystem resilience during drought. Nature 561, 538–541. https://doi.org/10/gd7gjf~~

~~Berg, A., Findell, K., Lintner, B., Giannini, A., Seneviratne, S.I., van den Hurk, B., Lorenz, R., Pitman, A., Hagemann, S., Meier, A., Cheruy, F., Ducharne, A., Malyshev, S., Milly, P.C.D., 2016. Land–atmosphere feedbacks amplify aridity increase over land under global warming. Nature Clim Change 6, 869–874. https://doi.org/10/f83mrn~~

~~Buck, A.L., 1981. New Equations for Computing Vapor Pressure and Enhancement Factor.~~

~~Chen, H., Wei, Y., Huang, J.J., 2024. Widespread increase in plant transpiration driven by global greening. Global and Planetary Change 235, 104395. https://doi.org/10/g9hg5j~~

~~Chen, H., Zhu, G., Shang, S., Qin, W., Zhang, Y., Su, Y., Zhang, K., Zhu, Y., Xu, C.,~~

2022. Uncertainties in partitioning evapotranspiration by two remote sensing-based models. Journal of Hydrology 604, 127223. https://doi.org/10/gsm5rt

Cheng, K., Yang, H., Guan, H., Ren, Y., Chen, Y., Chen, M., Yang, Z., Lin, D., Liu, W., Xu, J., Xu, G., Ma, K., Guo, Q., 2024. Unveiling China's natural and planted forest spatial–temporal dynamics from 1990 to 2020. ISPRS Journal of Photogrammetry and Remote Sensing 209, 37–50. https://doi.org/10.1016/j.isprsjprs.2024.01.024

Cheng, K., Zhang, Y., Yang, H., Ren, Y., Xiang, T., Chen, Y., Yang, Z., Chen, M., Xu, J., Huang, G., Xu, G., Tao, S., Yu, Z., Guo, Q., 2025. China's naturally regenerated forests currently have greater aboveground carbon accumulation rates than newly planted forests. Commun Earth Environ 6, 345. https://doi.org/10/hbbn33

Denissen, J.M.C., Teuling, A.J., Pitman, A.J., Koirala, S., Migliavacca, M., Li, W., Reichstein, M., Winkler, A.J., Zhan, C., Orth, R., 2022. Widespread shift from ecosystem energy to water limitation with climate change. Nat. Clim. Change 12, 677–684. https://doi.org/10.1038/s41558-022-01403-8

Fan, Y., Miguez-Macho, G., Jobbágy, E.G., Jackson, R.B., Otero-Casal, C., 2017. Hydrologic regulation of plant rooting depth. Proc. Natl. Acad. Sci. 114, 10572–10577. https://doi.org/10.1073/pnas.1712381114

Farley, K.A., Jobbágy, E.G., Jackson, R.B., 2005. Effects of afforestation on water yield: a global synthesis with implications for policy. Global Change Biology 11, 1565–1576. https://doi.org/10/dk34cg

Forrester, D.I., 2015. Transpiration and water-use efficiency in mixed-species forests versus monocultures: effects of tree size, stand density and season. Tree Physiol 35, 289–304. https://doi.org/10/f7c9tm

Fu, Z., Ciais, P., Feldman, A., Gentine, P., Makowski, D., Prentice, I.C., Stoy, P.C., 2022. Critical soil moisture thresholds of plant water stress in terrestrial ecosystems. Science Advances 8, eabq7827. https://doi.org/10/grrtgr

Grossiord, C., Buckley, T.N., Cernusak, L.A., Novick, K.A., Poulter, B., Siegwolf, R.T.W., Sperry, J.S., McDowell, N.G., 2020. Plant responses to rising vapor pressure deficit. New Phytologist 226, 1550–1566. https://doi.org/10.1111/nph.16485

Hirschi, M., Stradiotti, P., Crezee, B., Dorigo, W., Seneviratne, S.I., 2025. Potential of long-term satellite observations and reanalysis products for characterising soil drying: trends and drought events. Hydrology and Earth System Sciences 29, 397–425. https://doi.org/10/g9976b

Hu, Y., Wei, F., Fu, B., Zhang, W., Sun, C., 2023. Ecosystems in China have become more sensitive to changes in water demand since 2001. Commun Earth Environ 4, 444. https://doi.org/10/hbbnn2

Huang, X., Liang, S., Ziegler, A.D., Zeng, Z., 2025. Decoupling vegetation and soil-moisture interaction in evapotranspiration interannual variability. iScience 28, 113008. https://doi.org/10/hbbn34

Intergovernmental Panel on Climate Change (IPCC) (Ed.), 2023. Weather and Climate Extreme Events in a Changing Climate, in: Climate Change 2021 – The Physical Science Basis: Working Group I Contribution to the Sixth Assessment Report of the Intergovernmental Panel on Climate Change. Cambridge University Press, Cambridge, pp. 1513–1766. https://doi.org/10.1017/9781009157896.013

Jin, Z., You, Q., Zuo, Z., Li, M., Sun, G., Pepin, N., Wang, L., 2023. Weakening amplification of grassland greening to transpiration fraction of evapotranspiration over the Tibetan Plateau during 2001-2020. Agricultural and Forest Meteorology 341, 109661. https://doi.org/10/g9bfk4

Keenan, T.F., Hollinger, D.Y., Bohrer, G., Dragoni, D., Munger, J.W., Schmid, H.P., Richardson, A.D., 2013. Increase in forest-water-use efficiency as atmospheric carbon dioxide concentrations rise. Nature 499, 324–327. https://doi.org/10/f449vg

Keenan, T.F., Prentice, I.C., Canadell, J.G., Williams, C.A., Wang, H., Raupach, M., Collatz, G.J., 2016. Recent pause in the growth rate of atmospheric CO2 due to enhanced terrestrial carbon uptake. Nat Commun 7, 13428. https://doi.org/10/f8936d

Koehler, T., Wankmüller, F.J.P., Sadok, W., Carminati, A., 2023. Transpiration response to soil drying versus increasing vapor pressure deficit in crops: physical and physiological mechanisms and key plant traits. J Exp Bot 74, 4789–4807. https://doi.org/10/g8w6qp

Konings, A.G., Williams, A.P., Gentine, P., 2017. Sensitivity of grassland productivity to aridity controlled by stomatal and xylem regulation. Nature Geosci 10, 284–288. https://doi.org/10/f92qx5

Lavergne, A., Graven, H., De Kauwe, M.G., Keenan, T.F., Medlyn, B.E., Prentice, I.C., 2019. Observed and modelled historical trends in the water use efficiency of plants and ecosystems. Global Change Biology 25, 2242–2257. https://doi.org/10/gf3vmp

Li, C., Han, J., Liu, Z., Tu, Z., Yang, H., 2024. A harmonized global gridded transpiration product based on collocation analysis. Sci Data 11, 604. https://doi.org/10/g9gw9m

Lian, X., Piao, S., Li, L.Z.X., Li, Y., Huntingford, C., Ciais, P., Cescatti, A., Janssens, I.A., Peñuelas, J., Buermann, W., Chen, A., Li, X., Myneni, R.B., Wang, X., Wang, Y., Yang, Y., Zeng, Z., Zhang, Y., McVicar, T.R., 2020. Summer soil drying exacerbated by earlier spring greening of northern vegetation. Sci. Adv. 6, eaax0255. https://doi.org/10.1126/sciadv.aax0255

Liang, X., Wang, D., Ye, Q., Zhang, J., Liu, M., Liu, H., Yu, K., Wang, Y., Hou, E., Zhong, B., Xu, L., Lv, T., Peng, S., Lu, H., Sicard, P., Anav, A., Ellsworth, D.S., 2023. Stomatal responses of terrestrial plants to global change. Nat Commun 14, 2188. https://doi.org/10/gsdfj2

Liu, L., Gudmundsson, L., Hauser, M., Qin, D., Li, S., Seneviratne, S.I., 2020. Soil moisture dominates dryness stress on ecosystem production globally. Nat. Commun. 11, 4892. https://doi.org/10.1038/s41467-020-18631-1

Liu, Y., Kumar, M., Katul, G.G., Feng, X., Konings, A.G., 2020. Plant hydraulics accentuates the effect of atmospheric moisture stress on transpiration. Nat. Clim. Chang. 10, 691–695. https://doi.org/10/gpg5zk

Liu, Y., Lin, Z., Wang, Zijun, Chen, X., Han, P., Wang, B., Wang, Zhenqian, Wen, Z., Shi, H., Zhang, Z., Zhang, W., 2023. Discriminating the impacts of vegetation greening and climate change on the changes in evapotranspiration and transpiration fraction over the Yellow River Basin. Science of The Total Environment 904, 166926. https://doi.org/10/gs264j

Liu, Y., Wang, Y., Zhao, Y., Chen, S., Wang, L., Yang, W., Li, Xing, Li, Xinxi, Lei, H.,

Chang, H., Zhai, J., Zhu, Y., Wang, Q., Ye, T., 2025. Evapotranspiration stress intensifies with enhanced sensitivity to soil moisture deficits in a rapidly greening China. Hydrology and Earth System Sciences 29, 3379–3404. https://doi.org/10/g9975z

Martínez-Vilalta, J., Garcia-Forner, N., 2017. Water potential regulation, stomatal behaviour and hydraulic transport under drought: deconstructing the iso/anisohydric concept. Plant, Cell & Environment 40, 962–976. https://doi.org/10/gg6k7r

McDowell, N.G., Sapes, G., Pivovaroff, A., Adams, H.D., Allen, C.D., Anderegg, W.R.L., Arend, M., Breshears, D.D., Brodribb, T., Choat, B., Cochard, H., De Cáceres, M., De Kauwe, M.G., Grossiord, C., Hammond, W.M., Hartmann, H., Hoch, G., Kahmen, A., Klein, T., Mackay, D.S., Mantova, M., Martínez-Vilalta, J., Medlyn, B.E., Mencuccini, M., Nardini, A., Oliveira, R.S., Sala, A., Tissue, D.T., Torres-Ruiz, J.M., Trowbridge, A.M., Trugman, A.T., Wiley, E., Xu, C., 2022. Mechanisms of woody-plant mortality under rising drought, CO2 and vapour pressure deficit. Nat Rev Earth Environ 3, 294–308. https://doi.org/10/grz6gb

Niu, Z., He, H., Zhu, G., Ren, X., Zhang, L., Zhang, K., 2020. A spatial-temporal continuous dataset of the transpiration to evapotranspiration ratio in China from 1981–2015. Sci Data 7, 369. https://doi.org/10/gh3225

Novick, K.A., Ficklin, D.L., Stoy, P.C., Williams, C.A., Bohrer, G., Oishi, A.C., Papuga, S.A., Blanken, P.D., Noormets, A., Sulman, B.N., Scott, R.L., Wang, L., Phillips, R.P., 2016. The increasing importance of atmospheric demand for ecosystem water and carbon fluxes. Nature Clim Change 6, 1023–1027. https://doi.org/10/f9dpkn

Qing, Y., Wang, S., Ancell, B.C., Yang, Z.-L., 2022. Accelerating flash droughts induced by the joint influence of soil moisture depletion and atmospheric aridity. Nat Commun 13, 1139. https://doi.org/10/gpp55b

Schlesinger, W.H., Jasechko, S., 2014. Transpiration in the global water cycle. Agricultural and Forest Meteorology 189–190, 115–117. https://doi.org/10/gbfxc6

Song, J., Zhou, S., Yu, B., Li, Y., Liu, Y., Yao, Y., Wang, S., Fu, B., 2024. Serious underestimation of reduced carbon uptake due to vegetation compound droughts. npj Clim Atmos Sci 7, 1–11. https://doi.org/10/gtgssg

Sperry, J.S., Venturas, M.D., Anderegg, W.R.L., Mencuccini, M., Mackay, D.S., Wang, Y., Love, D.M., 2017. Predicting stomatal responses to the environment from the optimization of photosynthetic gain and hydraulic cost. Plant, Cell & Environment 40, 816–830. https://doi.org/10/f9jprm

Stoy, P.C., El-Madany, T.S., Fisher, J.B., Gentine, P., Gerken, T., Good, S.P., Klosterhalfen, A., Liu, S., Miralles, D.G., Perez-Priego, O., Rigden, A.J., Skaggs, T.H., Wohlfahrt, G., Anderson, R.G., Coenders-Gerrits, A.M.J., Jung, M., Maes, W.H., Mammarella, I., Mauder, M., Migliavacca, M., Nelson, J.A., Poyatos, R., Reichstein, M., Scott, R.L., Wolf, S., 2019. Reviews and syntheses: Turning the challenges of partitioning ecosystem evaporation and transpiration into opportunities. Biogeosciences 16, 3747–3775. https://doi.org/10/gf9p7s

Sun, S., Liu, Yibo, Chen, H., Ju, W., Xu, C.-Y., Liu, Yi, Zhou, B., Zhou, Yang, Zhou, Yanlian, Yu, M., 2022. Causes for the increases in both evapotranspiration and water yield over vegetated mainland China during the last two decades. Agricultural and Forest Meteorology 324, 109118. https://doi.org/10/gtcd5n

Wei, Z., Yoshimura, K., Wang, L., Miralles, D.G., Jasechko, S., Lee, X., 2017. Revisiting the contribution of transpiration to global terrestrial evapotranspiration. Geophysical Research Letters 44, 2792–2801. https://doi.org/10/gjkprx

Weiwei, L.U., Xinxiao, Y.U., Guodong, J.I.A., Hanzhi, L.I., Ziqiang, L.I.U., 2018. Responses of Intrinsic Water-use Efficiency and Tree Growth to Climate Change in Semi-Arid Areas of North China. Sci Rep 8, 308. https://doi.org/10/ghvh9v

Xu, H., Yue, C., Zhang, Y., Liu, D., Piao, S., 2023. Forestation at the right time with the right species can generate persistent carbon benefits in China. Proc Natl Acad Sci U S A 120, e2304988120. https://doi.org/10.1073/pnas.2304988120

Xu, L., Chen, N., Zhang, X., 2019. Global drought trends under 1.5 and 2 °C warming. International Journal of Climatology 39, 2375–2385. https://doi.org/10/gh35zt

Yuan, W., Zheng, Y., Piao, S., Ciais, P., Lombardozzi, D., Wang, Y., Liu, Y., Chen, G., Dong, W., Hu, Z., Jain, A.K., Jiang, C., Kato, E., Li, S., Lienert, S., Liu, S., Nabel, J.E.M.S., Qin, Z., Quine, T., Sitch, S., Smith, W.K., Wang, F., Wu, C., Xiao, Z., 2019. Increased atmospheric vapor pressure deficit reduces global vegetation growth. Science Advances 5, eaax1396. https://doi.org/10/gf6gm5

Zahra, N., Hafeez, M.B., Kausar, A., Al Zeidi, M., Asekova, S., Siddique, K.H.M., Farooq, M., 2023. Plant photosynthetic responses under drought stress: Effects and management. Journal of Agronomy and Crop Science 209, 651–672. https://doi.org/10/g9hmkv

Zhang, J., Liu, N., Zhang, C., Zhang, X., He, X., Jiang, W., Li, J., Zhan, Z., Peng, D., Lv, D., Ni, S., 2025. Deep soil moisture has limited impact on mitigating drought stress effects on plant transpiration in a subtropical secondary forest. Plant Soil 514, 427–444. https://doi.org/10/g9bfvc

Zhang, K., Chen, H., Ma, N., Shang, S., Wang, Y., Xu, Q., Zhu, G., 2024. A global dataset of terrestrial evapotranspiration and soil moisture dynamics from 1982 to 2020. Sci Data 11, 1–16. https://doi.org/10.1038/s41597-024-03271-7

Zhou, S., Yu, B., 2025. Neglecting land–atmosphere feedbacks overestimates climate-driven increases in evapotranspiration. Nat. Clim. Chang. 15, 1099–1106. https://doi.org/10/g93qz7

Zhou, S., Zhang, Y., Park Williams, A., Gentine, P., 2019. Projected increases in intensity, frequency, and terrestrial carbon costs of compound drought and aridity events. Sci. Adv. 5, eaau5740. https://doi.org/10.1126/sciadv.aau5740